Dynamics of Vehicles Subjected to Road Irregularities

by

Paraschoudis Athanasios & Xanthopoulou Natalia

with Thesis Supervisor, Dr. Costas Papadimitriou

A Thesis Submitted To

University of Thessaly, Department of Mechanical Engineering

and Division of Manufacturing, Materials & Constructions

in Partial Fulfillment of the Requirements for

the Degree of Diploma in Mechanical Engineering

March 2024, Greece

Approved by the Committee on Final Examination:

1. Prof. Costas Papadimitriou
   Professor of Structural Dynamics
   Department of Mechanical Engineering, University of Thessaly, GR
   email: costasp@uth.gr

2. Prof. Anastasios Stamatelos
   Professor of Internal Combustion Engines
   Department of Mechanical Engineering, University of Thessaly, GR
   email: stam@uth.gr

3. Assoc. Prof. Konstantinos Ampountolas
   Professor of Automatic Control Systems in Mechanical Engineering
   Department of Mechanical Engineering, University of Thessaly, GR
   email: k.ampountolas@uth.gr

Acknowledgements

This Diploma Thesis is written after a study conducted at the department of Mechanical Engineering of University of Thessaly.

First of all, we would like to thank our supervisor, Prof. Costas Papadimitriou, for his guidance and support during our research. To our colleagues Dr. Panagiotis Natsiavas, Orestis Giagkas Beltratis and Spyridon Mallios we owe our gratitude for their assistance and technical support on the development of the Multi-Body system.

We express our thanks to the examination committee of our thesis, Prof. Anastasios Stamatelos and Assoc. Prof. Konstantinos Ampountolas.

A warm appreciation to our friends Panos, Christina, Giannis, Stergios, Kostas and Marios for their motivation and encouragement. We've met as members of the formula student team and we 've shared great memories together. From moments of high pressure to moments of joy and celebration, this experience wouldn't have been the same without them.

Cheers to all our teammates in Centaurus Racing Team for the years we 've spent together and the great things we 've achieved. Our best wishes for the next generations.

Above all, we are grateful for our families, for their continuous support and love through our all these years and personal efforts to reach our goals.

"You can't connect the dots looking forward,
you can only connect them looking backwards.
You have to trust that the dots will somehow connect in your future.
You have to trust in something…your gut, destiny, life, karma…whatever,
because believing that the dots will connect down the road,
will give you the confidence to follow your heart,
even when it leads you off the well – worn path
and that will make all the difference…"

Steve Jobs

Contents

List of figures

List of tables

ABSTRACT

The scope of this Diploma Thesis is to investigate the interaction between a moving suspended vehicle and a simplified bridge or a rigid road under the effect of various road irregularities. The study focuses on the interaction forces between the tire and the pavement surface, how they are transmitted to the other vehicle components and how the bridge subsystem responses. This assignment consists of two parts, a) the interaction between the 2D moving vehicle and a simply supported beam which represents the bridge (Vehicle Bridge Interaction - VBI) [1 – 4, 18 - 19] and b) the 3D multi-body representation of a Formula Student vehicle driven in a rigid road profile [34 - 37]. In both parts, the roughness of the surface is implemented as it is described by the Power Spectral Density (PSD) method [3]. The present work serves as foundation for a great range of applications, such as vehicle vibrations analysis, structural compliance of components, bridge vibrations, bridge structural integrity, moving suspended systems, road irregularities etc.

The VBI method was approached by generating 2 and 4 degrees of freedom (DOFs) suspended system consisting of the car body and the tires. Parallel with that, implementing Galerkin discretization from Finite Element theory, the supported beam model was established to represent the bridge sub-system. The mass, stiffness and damping matrices of both car and bridge subsystems were combined into a linear coupled equation of motion. The coupled system was solved by time integration applying the Newmark's -beta method with a custom algorithm into MATLAB coding environment [13].

The presented vehicle for the 3D representation is a Formula Student single seater from Centaurus Racing Team of University of Thessaly (2021-2022). The initial geometry of the components was extracted by CAD software and implemented to HyperWorks where properties, materials and connections were defined. The road profiles indicate a straight path where the surface roughness is categorized into classes from poor quality (Country Roads) up to high quality roads (Autobahn). These classes are based on parameters of PSD method that set the amplitude and the frequency of the external excitation.

The Multi-Body method was approached by simulation software. HyperWorks tools by Altair Engineering, Inc. supported all stages of the simulation process. Starting from the geometry clean up and meshing in HyperMesh, moving on to the connection of the components and the generation of the complete vehicle assembly in MotionView, the use of MotionSolve for time transient simulations and finally analyzing the results in HyperView and HyperGraph [35, 37].

Chapter 1

Introduction

1.1 Background and motivation

Vibration analysis constitutes a pivotal domain intersecting numerous aspects of engineering, owing to its profound implications for structural integrity and public safety. A critical topic is the examination of the dynamic interaction between vehicles and road surfaces. This study seeks to examine and explain the complexities involved in this interaction, aiming to understand its various consequences and develop solutions to reduce risks. By diving into the complexities of vehicle-road dynamics, we aim to deepen our understanding of this vital aspect of transportation engineering, ultimately improving the safety and resilience of infrastructure.

Road irregularities significantly impact vehicle dynamics and suspension performance. The suspension system of a vehicle serves to mitigate the effects of road imperfections, maintaining tire contact and vehicle stability. Understanding how vehicle suspension interacts with road irregularities and how the loads are transferred to the chassis of the car, is crucial for optimizing vehicle handling, comfort, and safety. The interaction between vehicle suspension and road irregularities is further complicated when vehicles traverse bridges [1 – 4, 18 - 19]. Bridge dynamics introduce additional factors such as structural stiffness, deck surface conditions, and dynamic loading patterns. The response of the vehicle under various road irregularities can provide comprehensive design parameters for itself and the bridge. Monitoring the vehicle is relatively easy while monitoring bridges is quite difficult and expensive. Utilizing vehicles as monitoring platforms for assessing both road irregularities and bridge dynamics offers a cost-effective and efficient solution. By equipping vehicles with sensors to measure loads and vibrations, valuable data can be gathered on the interaction between vehicles and bridges, without the need for extensive bridge monitoring infrastructure. Using potentiometers, accelerometers, gyroscopes, wheel speed sensors etc., a detailed analysis on the loads of the components can be achieved.

Integrating vehicle-based monitoring with multi-body simulation software facilitates the development of accurate models for studying the interaction between vehicles and bridges and provides feedback of the vibrations and the loads acting on the two systems [34 - 36]. By utilizing real-world data collected from vehicles equipped with sensors, engineers can refine and validate multi-body simulation models to accurately represent dynamic interactions. This approach enables comprehensive analysis of road irregularities, bridge dynamics, and vehicle behavior under regular phenomena, aiding in the design of more resilient infrastructure and advanced vehicle systems.

By extracting geometries directly from CAD software maintaining in this way all their design characteristics, the multi-body simulation captures precise details of vehicle structure and provides reliable results. In software like Altair MotionView [35, 37], we achieve to present a fully functional assembly of a formula student car. Its most vital structural components, chassis and suspension parts are flexible and absorb part of the external excitation caused by road irregularities. The development of such complicated systems has numerous applications in the field of transportation. Commercial vehicles and means of public transportation are developed to provide isolation in the cabin taking into account internal stimulators like the engines. As we move from a vehicle to a high-speed train or to an airplane the complexity and the load case change, but the efficiency of such simulations determines the final design.

1.2 Outline

This study undertakes a comprehensive examination of two critical aspects: the Vehicle Bridge Interaction (VBI) problem and the influence of road irregularities on the dynamics of moving vehicles. The primary objective is to develop a highly accurate model of vehicles to facilitate real-time calculations of their interactions with bridge structures.

In Chapter 2, particular emphasis is placed on the modeling of both bridges and vehicles. While the analytical and numerical aspects of bridge systems are explored, the thesis primarily focuses on numerical methods. Two distinct types of vehicles are selected for simulation purposes: one featuring 2 degrees of freedom (DOFs), and the other with 4 DOFs. It's imperative to account for road irregularities as they play a significant role in determining the external loads acting on vehicles. The derivation of equations of motion for the main systems and their internal components involves the utilization of free body diagrams. Furthermore, finite element analysis is conducted for the bridge system using the Galerkin method. The coupled system's solution is tackled through the implementation of Newmark's-β method, executed within a MATLAB coding environment.

Moving on to Chapter 3, an extensive overview of the fundamental suspension and tire characteristics of real single-seater vehicles is provided. The aim is to construct a detailed model within the framework of multibody software. This model is subjected to various classes of roughness in road profiles to comprehensively evaluate the stresses exerted on vehicle components and the overall dynamic behavior under external loading conditions.

Finally, Chapter 4 summarizes the conclusions drawn from the research. Additionally, it presents aspects for future research and directions of further investigation of the presented subject.

Chapter 2

Vehicle Bridge Interaction (VBI)

2.1 Introduction

The analysis conducted in this chapter refers to a 2D representation of two systems, the vehicle and the bridge [2 – 5, 14 – 17, 22]. The analysis was done using MATLAB, describing the equations of motion of both, as the vehicle is travelling at constant speed.

The vehicle's subsystem consists of the car body and one tire on each axle. Both the tires and the body move in vertical direction and the latter also rotates around the lateral axis passing from the center of mass. The vehicle's subsystem has in total four degrees of freedom. The bridge subsystem is a simple supported Euler - Bernoulli beam which mathematical model is described using Finite Element Methods and solved implementing the Galerkin method. The damping of the bridge is calculated through Rayleigh's method.

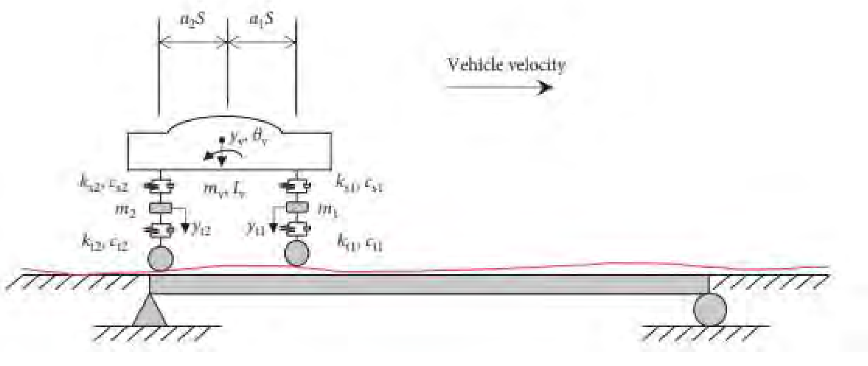

Figure 2.1: Vehicle bridge model representation.

Road roughness is added as stationary Gaussian random process with zero-mean value wherein roughness can be characterized by its Power Spectral Density (PSD).

2.2 Bridge subsystem

2.2.1 Equation of motion - analytical approach

Considering the dynamic load $q(x,t)$ and implementing an Euler-Bernoulli simply supported beam to represent the bridge the problem is formulated as next figure shows [6].

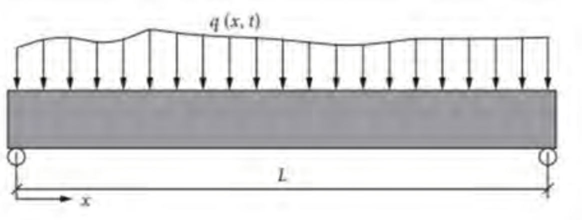

Figure 2.2: External load on the Euler - Bernoulli beam.

The length of the beam is L and the width is unit, the density is ϱ(x) and the cross-sectional area is A(x), the young modulus is E and the area moment of inertia is I. Isolating a small segment of the beam with length dx the free body diagram is representing below. The damping force due to the bridge is defined as $c\frac{\partial u}{\partial t}$. The M(x,t) and M(x+dx,t) signify the moment acting on the left and right cross section respectively. Q(x,t) and Q(x+dx,t) signify the vertical force acting on the left and right cross section respectively. The axial forces are neglected and therefore $N(x,t) = 0$.

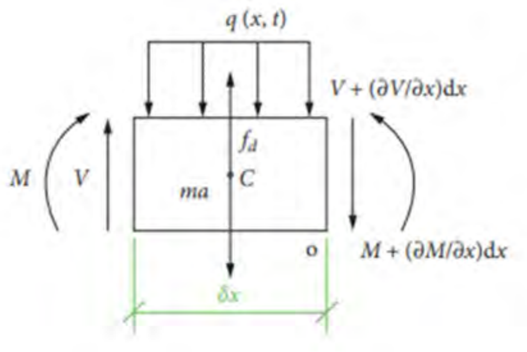

Figure 2.3: Infinitesimal segment load analysis

Newton's equation of motion is written as:

$$\sum F_y = \rho(x) \cdot A(x) \cdot dx \cdot \frac{\partial^2 u(x,t)}{\partial x^2} \qquad [2.1]$$

$$Q(x,t)\cdot\cos(\theta(x,t))-Q(x+dx,t)\cdot\cos(\theta(x+dx,t))+q(x,t)\cdot dx-c\frac{\partial u}{\partial t}\cdot dx=\rho(x)\cdot A(x)\cdot dx\cdot\frac{\partial^2 u(x,t)}{\partial t^2} \quad [2.2]$$

Applying Taylor's theorem, equation [2.2] is transformed into:

$$-\frac{\partial Q(x,t)}{\partial x}+q(x,t)-c\cdot\frac{\partial u}{\partial t}=\rho(x)\cdot A(x)\cdot\frac{\partial^2 u(x,t)}{\partial t^2} \quad [2.3]$$

The 2nd Euler's law leads to the second fundamental equation of the analytical approach.

$$\sum M = I\cdot dx\cdot\frac{\partial^2\theta(x,t)}{\partial t^2} \quad [2.4]$$

$$M(x,t)-M(x+dx,t)-Q(x,t)\cdot dx-q(x,t)\cdot dx\cdot\frac{dx}{2}=I\cdot dx\cdot\frac{\partial^2\theta(x,t)}{\partial t^2} \quad [2.5]$$

Applying Taylor's theorem, equation [2.5] is transformed into:

$$-\frac{\partial M(x,t)}{\partial x}-Q(x,t)=I\cdot dx\cdot\frac{\partial^2\theta(x,t)}{\partial t^2} \quad [2.6]$$

For beams that satisfy the relation h<<L the inertial term due to rotation is neglected.

$$Q(x,t)=-\frac{\partial M(x,t)}{\partial x} \quad [2.7]$$

Implementing the constitutive law for linear elastic material:

$$M(x,t)=-EI\cdot\frac{\partial^2 u(x,t)}{\partial x^2} \quad [2.8]$$

and combining with the equation [2.7] and considering a uniform beam with constant EI and $\rho\cdot A$, the equation [2.1] now can be written as:

$$-EI\cdot\frac{\partial^4 u(x,t)}{\partial x^4}+q(x,t)-c\cdot\frac{\partial u(x,t)}{\partial t}=\rho\cdot A\cdot\frac{\partial^2 u(x,t)}{\partial t^2} \quad [2.9]$$

Equivalently,

$$EI\cdot\frac{\partial^4 u(x,t)}{\partial x^4}+\rho\cdot A\cdot\frac{\partial^2 u(x,t)}{\partial t^2}+c\cdot\frac{\partial u(x,t)}{\partial t}=q(x,t) \quad [2.10]$$

In the last form, $\rho\cdot A$, EI, c represent the mass, the stiffness and the damping of the beam respectively.

2.2.1.1 Modal analysis

To conduct modal analysis on the bridge, the equation of motion of an undamped oscillated beam is implemented.

$$-EI \cdot \frac{\partial^4 u(x,t)}{\partial x^4} + q(x,t) = \rho \cdot A \cdot \frac{\partial^2 u(x,t)}{\partial t^2} \quad [2.11]$$

The homogenous part is isolated.

$$-EI \cdot \frac{\partial^4 u(x,t)}{\partial x^4} = \rho \cdot A \cdot \frac{\partial^2 u(x,t)}{\partial t^2} \quad [2.12]$$

Employing method of separation variables at the homogenous linear partial differential equation [2.12], the initial response is assumed to be $u(x,t) = X(x)T(t)$. The derivatives of $u(x,t)$ are,

$$\frac{\partial^2 u(x,t)}{\partial t^2} = X(x)\ddot{T}(t) \quad [2.13]$$

$$\frac{\partial^4 u(x,t)}{\partial x^4} = X''''(x)T(t) \quad [2.14]$$

The equation of motion [2.10] is now transformed.

$$-EI \cdot X''''(x) \cdot T(t) + \rho \cdot A \cdot X(x) \cdot \ddot{T}(t) = 0 \quad [2.15]$$

$$-\frac{EIX''''(x)T(t)}{\rho \cdot A \cdot X(x)T(t)} + \frac{\rho \cdot A \cdot X(x)\ddot{T}(t)}{\rho \cdot A \cdot X(x)T(t)} = 0 \quad [2.16]$$

$$-\frac{EIX''''(x)}{\rho \cdot A \cdot X(x)} = -\frac{\ddot{T}(t)}{T(t)} = -\omega^2 \quad [2.17]$$

$$EIX''''(x) - \omega^2 \rho \cdot A \cdot X(x) = 0 \quad [2.18]$$

The equation [2.18] describes the 4th order eigenproblem. Four boundary conditions are demanded for the solution.

For a simply supported beam the boundary conditions are,

$$u(x=0,t) = 0 \Rightarrow X(0) = 0 \quad [2.19]$$

$$u(x=L,t) = 0 \Rightarrow X(L) = 0 \quad [2.20]$$

$$M(x=0,t) = 0 \Rightarrow u''(0,t) = 0 \Rightarrow X''(0) = 0 \quad [2.21]$$

$$M(L,t)=0 \Rightarrow u''(L,t)=0 \Rightarrow X''(L)=0 \quad [2.22]$$

Introducing the $s^4 = \frac{\omega^2 \rho A}{EI}$ the equation [2.18] becomes,

$$X''''(x) - s^4 X(x) = 0 \quad [2.23]$$

The solution of the eigenvalue problem is,

$$X(x) = a \cdot cos(s \cdot x) + \beta \cdot \sin(s \cdot x) + \gamma \cdot cosh(s \cdot x) + \delta \cdot \sinh(s \cdot x) \quad [2.24]$$

The combination of the boundary conditions and the solution results in an algebraic system. The solution of the system leads to eigenvalues and eigenfunctions.

$$\omega_r = \frac{r^2 \pi}{L^2} \sqrt{\frac{EI}{\rho \cdot A}} \qquad , r = 1, 2, \ldots, n \quad [2.25]$$

$$X_r(x) = \sin(\frac{r \pi x}{L}) \quad [2.26]$$

The normalized eigenfunctions are occurred using the orthogonality rule,

$$\hat{m}_r(x) = \int_0^L \rho \cdot A \cdot X_r^2(x) dx = \frac{\rho \cdot A \cdot L}{2} \quad [2.27]$$

as,

$$\varphi_r(x) = \sqrt{\frac{2}{\rho \cdot \mathrm{A} \cdot L}} \cdot \sin\left(\frac{r \pi x}{L}\right) \quad [2.28]$$

The normalized eigenfunctions form a basis for the space of eigenfunctions that satisfy the boundary conditions of the problem. Consequently, each function $u(x)$ that satisfies the boundary conditions can be written as,

$$u(x) = \sum_{r=1}^{\infty} a_r \Phi_r(x) \quad [2.29]$$

$with\ a_r = \int_0^L \rho A \Phi_r(x) u(x)\, dx$

Suppose a solution in the form,

$$u(x,t) = \sum_{r=1}^{\infty} \xi_r(t) \Phi_r(x) \quad [2.30]$$

Replace the solution [2.30] to the equation [2.11],

$$-\sum_{r=1}^{\infty} \xi_r \cdot EI \cdot \Phi_r''''(x) + q(x,t) = \rho \cdot A \cdot \sum_{r=1}^{\infty} \ddot{\xi}_r \cdot \Phi_r(x) \quad [2.31]$$

Recalling the equations [2.18] and [2.28],

$$\ddot{\xi}_r(t) + \omega_r^{\,2} \cdot \xi_r(t) = \hat{q}_r \quad [2.32]$$

Where, $\hat{q}_r = \int_0^L q(x,t)\Phi_r(x)\,dx$, r = 1,2 … n

Adding the damping contribution, the final shape of the eigenvalue equation is,

$$\ddot{\xi}_r(t) + 2 \cdot \zeta_r \cdot \omega_r \cdot \dot{\xi}_r(t) + \omega_r^{\,2} \cdot \xi_r(t) = \hat{q}_r \quad [2.33]$$

With initial conditions,

$$\xi_r(0) = \int_0^L \rho \cdot A \cdot \Phi_r(x) \cdot u(x,0)dx \quad [2.34]$$

$$\dot{\xi}_r(0) = \int_0^L \rho \cdot A \cdot \Phi_r(x) \cdot \dot{u}(x,0)dx \quad [2.35]$$

2.2.1.2 Moving load effect

The simplest example for analysis bridge's response under moving load is the one of single point constant force P_o [6]. So, the force is defined as,

$$q(x,t) = P_0 \cdot \delta(x - x_0) = P_0 \cdot \delta(x - v_0 \cdot t) \quad [2.36]$$

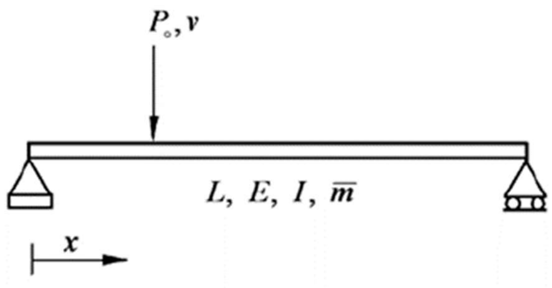

Figure 2.4: Moving load effect

As previously described the solution has the shape $u(x,t) = \sum_{r=1}^{\infty} \xi_r(t)\Phi_r(x)$ with the time response $\xi_r(t)$ defined by the eigenvalue's equation.

$$\ddot{\xi}_r(t) + 2 \cdot \zeta_r \cdot \omega_r \cdot \dot{\xi}_r(t) + \omega_r^{\,2} \cdot \xi_r = \hat{q}_r \quad [2.37]$$

Replacing the load $q(x,t)$ from the equation [2.36] into $\hat{q}_r = \int_0^L q(x,t)\Phi_r(x)\,dx$, $\hat{q}_r$ is calculated.

$$\hat{q}_r = P_0 \cdot \Phi_r(x_0) = P_0 \cdot \sqrt{\frac{2}{\rho \cdot A \cdot L}} \cdot \sin\left(\frac{r \cdot \pi \cdot x_0}{L}\right) \quad [2.38]$$

Or,

$$\hat{q}_r = P_0 \cdot \sqrt{\frac{2}{\rho \cdot A \cdot L}} \cdot \sin\left(\frac{r \cdot \pi \cdot v_0}{L} \cdot t\right) \quad [2.39]$$

The response of the vibration equation [2.33] is,

$$\xi_r(t) = X(\eta_r, \zeta_r) \cdot P_0 \cdot \frac{\sqrt{\frac{2}{\rho \cdot A \cdot L}}}{\omega_r^{\,2}} \cdot \sin(\Omega_r \cdot t - \varphi_r) \quad [2.40]$$

Where,

- $\tan(\varphi_r) = \frac{2\zeta_r\eta_r}{1-\eta_r^{\,2}}$
- frequency vibration is $\eta_r = \frac{\Omega_r}{\omega_r}$
- the excitation frequency is $\Omega_r = \frac{r\pi v_0}{L}$

The excitation frequency is directly affected by the body's vehicle.

2.2.2 Equation of motion - numerical approach

The discretized form of Bernoulli's beam consists of N nodes, so N-1 elements of equal length. Each node j has two degrees of freedom, the displacement $u_j = u(x_j, t)$ and the rotation $\theta_j = u'(x_j, t)$ [7].

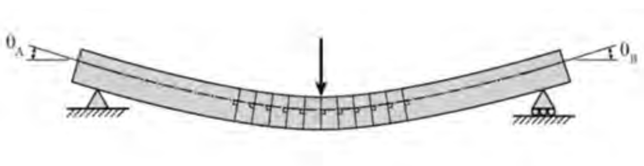

Figure 2.5: Deformation of the Bernoulli's beam

The equation of motion for the bridge's subsystem in matrix form has the following shape.

$$\boldsymbol{M}_B \cdot \{\ddot{\boldsymbol{u}}_B\} + \boldsymbol{C}_B \cdot \{\dot{\boldsymbol{u}}_B\} + \boldsymbol{K}_B \cdot \{\boldsymbol{u}_B\} = \{\boldsymbol{F}_B(t)\} \qquad [2.41]$$

The $\boldsymbol{M_b}$, $\boldsymbol{C_b}$, $\boldsymbol{K_b} \in \mathbb{R}^{\boldsymbol{2N\times 2N}}$ are the mass, damping and stiffness matrices respectively and they depend on the geometrical and structural characteristics of the bridge. The $\boldsymbol{F_b}(t)$ is the excitation force vector $\in \mathbb{R}^{\boldsymbol{2N\times 1}}$. The generation of the matrices and vectors is the result of the superposition of the local matrices $\in \mathbb{R}^{\boldsymbol{4\times 4}}$ and $\mathbb{R}^{\boldsymbol{4\times 1}}$ which are calculated inside each element to the corresponding global ones.

2.2.2.1 Galerkin discretization method

The "roof" functions $\varphi_j(x)$, j=1,2…$N-1$ are set below.

$$\varphi_j(x) = \frac{x - x_{j-1}}{x_j - x_{j-1}} \qquad , \; x_j \le x \le x_{j+1} \qquad [2.42]$$

$$\varphi_j(x) = \frac{x - x_{j+1}}{x_j - x_{j+1}} \qquad , \; x_{j-1} \le x \le x_j \qquad [2.43]$$

$$\varphi_j(x) = 0 \qquad , \; x \le x_{j-1} \qquad [2.44]$$

$$\varphi_j(x) = 0 \qquad , \; x \ge x_{j+1} \qquad [2.45]$$

or,

$$\varphi_i(x_j) = \delta_{ij} \cdot \begin{cases} 1, & i = j \\ 0, & i \ne j \end{cases} \qquad [2.46]$$

The Galerkin Method approaches the solution with linear combination of shape functions.

$$u(x,t) = \sum_{j=1}^{N} a_j(t) \cdot \varphi_j(x) \qquad [2.47]$$

For every node i it is assumed that

$$u(x_i,t) = \sum_{j=1}^{N} a_j(t) \cdot \varphi_j(x_i) = \sum_{j=1}^{N} a_j(t) \cdot \delta_{ij} = a_i(t) \qquad [2.48]$$

The Galerkin coefficients $a_i = a_i(t)$ are time dependent and represent the nodes displacement of the discretized problem.

The governing equation is known as:

$$m \cdot \frac{\partial^2 u(x,t)}{\partial t^2} + EI \cdot \frac{\partial^4 u(x,t)}{\partial x^4} = q(x,t) \qquad [2.49]$$

While the boundary conditions for the given beam are:

$$u(x=0,t)=0 \qquad [2.50]$$

$$u(x=L,t)=0 \qquad [2.51]$$

$$u'(x=0,t)=\theta_0 \qquad [2.52]$$

$$u'(x=L,t)=\theta_L \qquad [2.53]$$

The admissible function $u^*(x,t) = \sum_{j=1}^{N} a_j^* \cdot \varphi_i(x)$ is introduced to represent the approximation of the unknown solution.

The governing equation is formulated to the weak form of the problem.

$$\int_0^L \left(m \cdot \frac{\partial^2 u(x,t)}{\partial t^2} + EI \cdot \frac{\partial^4 u(x,t)}{\partial x^4} - q(x,t) \right) \cdot u^*(x,t) dx = 0 \qquad [2.54]$$

Now, applying twice factorial integration the weak form can be written as:

$$\left[EIu'''u^* \right]_0^L - \left[EIu''u^{*\prime} \right]_0^L + \int_0^L \left(m \cdot \ddot{u} \cdot u^* + EI \cdot u'' \cdot u^{*\prime\prime} - q \cdot u^* \right) dx = 0 \qquad [2.55]$$

Also, from the constitutive law for linear elastic material:

$$M(x,t) = -EI \cdot \frac{\partial^2 u(x,t)}{\partial x^2} \qquad [2.56]$$

$$x = L: \quad M(L,t) = -EI \cdot \frac{\partial^2 u(L,t)}{\partial x^2} = -M_L \qquad [2.57]$$

So,

$$u''(L,t) = \frac{M_L}{EI} = m_L \qquad [2.58]$$

$$x = 0: \quad M(0,t) = -EI \cdot \frac{\partial^2 u(0,t)}{\partial x^2} = -M_0 \qquad [2.59]$$

So,

$$u''(0,t) = \frac{M_0}{EI} = m_0 \qquad [2.60]$$

And therefore,

$$\int_0^L EI \cdot u'' \cdot u^{*''} dx = \int_0^L \left(qu^* - m\ddot{u}u^* \right) dx + EI \cdot \mathrm{m}_L \cdot \theta_L - EI \cdot \mathrm{m}_0 \cdot \theta_0 \quad [2.61]$$

Combining the symmetric weak form with the Galerkin function, the elements from mass and stiffness matrices and force vector are obtained.

$$M_{ij} = \int_0^L m \cdot \varphi_i \cdot \varphi_j dx \quad [2.62]$$

$$K_{ij} = \int_0^L EI \cdot \varphi_i'' \cdot \varphi_j'' dx \quad [2.63]$$

$$F_i = \int_0^L q \cdot \varphi_i dx - EI \cdot m_L \cdot \theta_L + EI \cdot m_0 \cdot \theta_0 \quad [2.64]$$

The sum of the translational and rotational displacement leads to the final vector $u(x)$.

$$u(x) = \sum_{i=1}^{N} u_i \cdot \varphi_i(x) + \sum_{i=1}^{N} \theta_i \cdot \tilde{\varphi}_i(x) \quad [2.65]$$

2.2.2.2 Local coordinate system

Between two nodes A and B with actual coordinates x_A, x_B a local system is generated starting from A $\xi_A = -1$ until B $\xi_B = 1$.

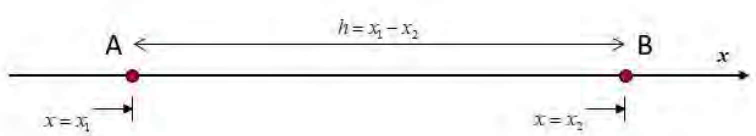

Figure 2.6: Global coordinates

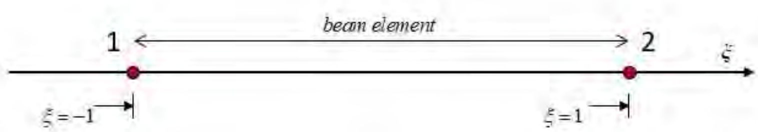

Figure 2.7: Local coordinates

The following transformation takes place.

$$x(\xi) = x_A + \frac{h}{2} \cdot (1+\xi) \qquad , \ -1 \le \xi \le 1 \tag{2.66}$$

Thus,

$$\xi = (x - x_A) \cdot \frac{2}{h} - 1 \tag{2.67}$$

Inside each element, there are only four non-zero shape functions that contribute in the equation [2.65].

$$u(x) = \varphi^e{}_A(x) \cdot u_A + \tilde{\varphi}^e_A(x) \cdot \theta_A + \varphi^e{}_B(x) \cdot u_B + \tilde{\varphi}^e_B(x) \cdot \theta_B \tag{2.68}$$

The local displacement vector $\boldsymbol{u^e}$ consists of four variables. In relation to the global system is defined with u_A, θ_A, u_B, θ_B.

Figure 2.8: Local displacement vector components

$$\{\mathbf{u}^e\} = \begin{bmatrix} u_A \\ \theta_A \\ u_\mathrm{B} \\ \theta_B \end{bmatrix} \tag{2.69}$$

Its transformation into the local coordinates system results in $u(\xi) = [\boldsymbol{N}(\xi)] \cdot \{\boldsymbol{u^e}\}$. Where $\boldsymbol{N(\xi)}$ is written below adopting a matrix notation.

$$[\boldsymbol{N}(\xi)] = [\mathrm{N}_1(\xi) \quad \mathrm{N}_2(\xi) \quad \mathrm{N}_3(\xi) \quad \mathrm{N}_4(\xi)] \tag{2.70}$$

The local displacement vector is represented below.

$$u(\xi) = N_1(\xi) \cdot u_A + N_2(\xi) \cdot \theta_A + N_3(\xi) \cdot u_\mathrm{B} + N_4(\xi) \cdot \theta_\mathrm{B} \tag{2.71}$$

The shape functions are reshaped as 3rd order polynomials with respect to ξ. Each polynomial $N_i(\xi) = c_{0i} + c_{1i} \cdot \xi + c_{2i} \cdot \xi^2 + c_{3i} \cdot \xi^3$ has to satisfy 4 kinematic limitations per element.

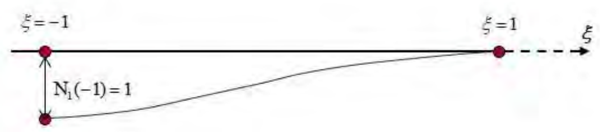

Figure 2.9: Transport kinematic constraint at ξ=-1

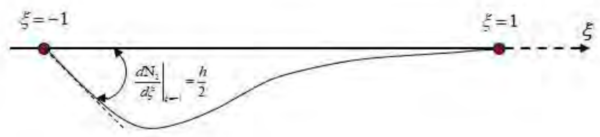

Figure 2.10: Rotational kinematic constraint at ξ=-1

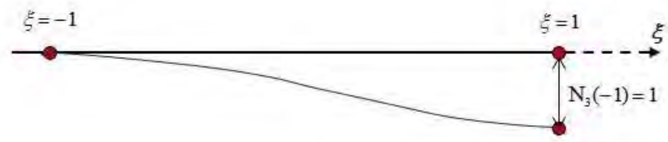

Figure 2.11: Transport kinematic constraint at ξ=1

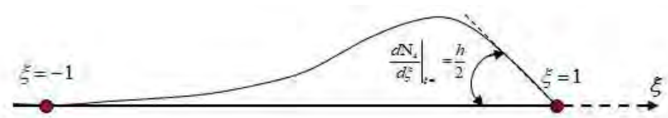

Figure 2.12: Rotational kinematic constraint at ξ=1

Their final form is.

$$N_1(\xi) = \frac{1}{4} \cdot (2 - 3 \cdot \xi + \xi^3) \quad [2.72]$$

$$N_2(\xi) = \frac{1}{8} \cdot (1 - \xi - \xi^2 + \xi^3) \quad [2.73]$$

$$N_3(\xi) = \frac{1}{4} \cdot (2 + 3 \cdot \xi - \xi^3) \quad [2.74]$$

$$N_4(\xi) = \frac{1}{8} \cdot (-1 - \xi + \xi^2 + \xi^3) \qquad [2.75]$$

The equations [2.62] and [2.63] become,

$$M_{ij} = \int_{x_A}^{x_B} m N_i N_j dx \qquad [2.76]$$

$$K_{ij} = \int_{x_A}^{x_B} EI N_i'' N_j'' dx \qquad [2.77]$$

The mass and stiffness matrices are transformed.

$$\left[\mathbf{M}^e\right] = \int_{-1}^{1} \left(m \cdot [\boldsymbol{N}]^T \cdot [\boldsymbol{N}] \cdot \frac{h}{2} \right) d\xi \qquad [2.78]$$

$$\left[\mathbf{K}^e\right] = \int_{-1}^{1} \left(EI \cdot [\boldsymbol{N}'']^T \cdot [\boldsymbol{N}''] \cdot \frac{h}{2} \right) d\xi \qquad [2.79]$$

And finally calculated as,

$$\left[\mathbf{M}^e\right] = \frac{m}{420} \begin{bmatrix} 156 & 22h & 54 & -13h \\ 22h & 4h^2 & 13h & -3h^2 \\ 54 & 13h & 156 & -22h \\ -13h & -3h^2 & -22h & 4h^2 \end{bmatrix} \qquad [2.80]$$

$$\left[\mathbf{K}^e\right] = \frac{EI}{h^3} \begin{bmatrix} 12 & 6h & -12 & 6h \\ 6h & 4h^2 & -6h & 2h^2 \\ -12 & -6h & 12 & -6h \\ 6h & 2h^2 & -6h & 4h^2 \end{bmatrix} \qquad [2.81]$$

Similarly, the external force vector of equation [2.64], is transformed to

$$\left\{\mathbf{F}^e\right\} = \int_{-1}^{1} \left(q(x(\xi), t) \cdot [\boldsymbol{N}]^T \cdot \frac{h}{2} \right) d\xi \qquad [2.82]$$

Considering the concentrated force Q acting from the tire's contact patch to a random point *a* inside any element of the bridge.

$$\{F^e\} = Q \cdot \begin{bmatrix} N_1(\xi_a) \\ N_2(\xi_a) \\ N_3(\xi_a) \\ N_4(\xi_a) \end{bmatrix} \quad , -1 \leq \xi_\alpha \leq 1 \tag{2.83}$$

2.2.2.3 Rayleigh damping method

The Rayleigh method is a viscous damping approximation and is mathematically described as a linear combination of mass and stiffness matrices of the construction [6, 15].

$$\boldsymbol{C} = a \cdot \boldsymbol{M} + \beta \cdot \boldsymbol{K} \tag{2.84}$$

The damping ratio and the frequency for two vibration modes are required to define the coefficients α and β, where α is the mass proportional and β is the stiffness proportional.

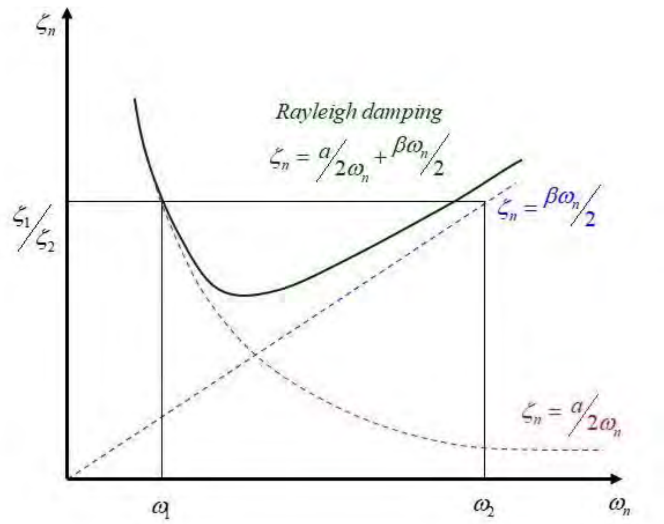

Figure 2.13: Rayleigh damping components

Rayleigh damping is grounded in the assumption that only the lower frequency modes of vibration are significant.

The equation of motion for a vibrating system is:

$$\frac{d^2u}{dt^2} + \frac{c}{m} \cdot \frac{du}{dt} + \frac{k}{m} \cdot u = \frac{f(t)}{m} \tag{2.85}$$

Substituting the Rayleigh equation into the equation of motion the latter is transformed into the below equation.

$$\frac{d^2u}{dt^2} + \left(a + \beta \cdot \omega_0{}^2\right) \cdot \frac{du}{dt} + \omega_0{}^2 \cdot u = \frac{f(t)}{m} \qquad [2.86]$$

And therefore, Rayleigh damping can be used to express the damping ratio experienced at the resonance point of the vibration,

$$\zeta = \frac{1}{2} \cdot \left(\frac{a}{\omega_0} + \beta \cdot \omega_0 \right) \qquad [2.87]$$

Each mode of the system corresponds to a different resonant frequency and hence in a different expression for the damping ratio.

So, for two of the lowest eigenfrequencies ω_1, ω_2 the damping ratios ζ_1, ζ_2 are matched and hence from the equation [2.87] the following system can be generated.

$$\begin{bmatrix} \zeta_1 \\ \zeta_2 \end{bmatrix} = \begin{bmatrix} \frac{1}{2} \cdot \left(\frac{a}{\omega_1} + \beta \cdot \omega_1 \right) \\ \frac{1}{2} \cdot \left(\frac{a}{\omega_2} + \beta \cdot \omega_2 \right) \end{bmatrix} \qquad [2.88]$$

$$\begin{cases} a = 4\pi f_1 f_2 \dfrac{\zeta_1 f_2 - \zeta_2 f_1}{f_2^2 - f_1^2} \\ \beta = \dfrac{\zeta_2 f_2 - \zeta_1 f_1}{\pi\left(f_2^2 - f_1^2\right)} \end{cases} \qquad [2.89]$$

2.3 Vehicle subsystem

2.3.1 Equation of motion of 2 - DOFs vehicle

Starting from a simplified representation of the moving sprung mass, a single wheel model is built. The system comprises a body and a wheel which are connected through suspension elements. Each part has one degree of freedom coming from their vertical movement and results in a total 2 degrees of freedom vehicle subsystem.

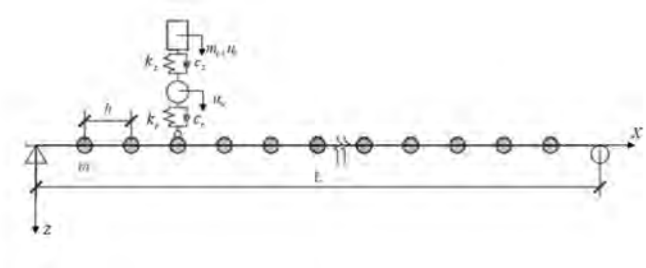

Figure 2.14: 2-DOF vehicle representation

The free body diagrams of the vehicle follow.

Car body:

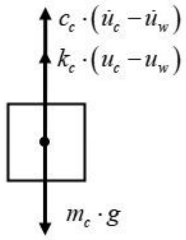

Figure 2.15: Free body diagram of car body

$$\sum F_c = m_c \cdot \ddot{u}_c$$

$$m_c \cdot \ddot{u}_c + c_c \cdot \dot{u}_c - c_c \cdot \dot{u}_w + k_c \cdot u_c - k_c \cdot u_w = m_c \cdot g \quad [2.90]$$

Wheel:

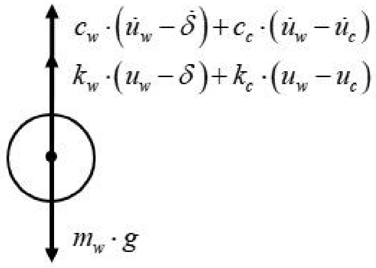

Figure 2.16: Free body diagram of the wheel

$$\sum F_w = m_w \cdot \ddot{u}_w$$

$$m_w \cdot \ddot{u}_w + (c_c + c_w) \cdot \dot{u}_w - c_c \cdot \dot{u}_c + (k_c + k_w) \cdot u_w - k_c \cdot u_c = c_w \cdot \dot{\delta} + k_w \cdot \delta + m_w \cdot g \quad [2.91]$$

Summarizing the equations of motion for the system the combined EOM is written below.

$$\begin{bmatrix} m_c & 0 \\ 0 & m_w \end{bmatrix}\begin{bmatrix} \ddot{u}_c \\ \ddot{u}_w \end{bmatrix}+\begin{bmatrix} c_c & -c_c \\ -c_c & c_c+c_w \end{bmatrix}\begin{bmatrix} \dot{u}_c \\ \dot{u}_w \end{bmatrix}+\begin{bmatrix} k_c & -k_c \\ -k_c & k_c+k_w \end{bmatrix}\begin{bmatrix} u_c \\ u_w \end{bmatrix}=\begin{bmatrix} m_c \cdot g \\ k_w \cdot \delta + m_w \cdot g \end{bmatrix} \qquad [2.92]$$

2.3.2 Equation of motion of 4 - DOFs vehicle

The subsystem consists of the car body and the two wheels. The mass of the car is connected through springs and shock absorbers with the wheels, and the wheels are always in contact with the road surface. The car body now has 2 degrees of freedom, a rotational around lateral axis and a translational around vertical axis, while each wheel moves aligned with the sprung mass. The model has in total 4 degrees of freedom and is represented in the figure below.

$$\{\boldsymbol{u}_v\} = \begin{bmatrix} u_c & \theta & u_{wf} & u_{wr} \end{bmatrix}^T = \begin{bmatrix} \boldsymbol{u}_c & \boldsymbol{u}_w \end{bmatrix}^T$$

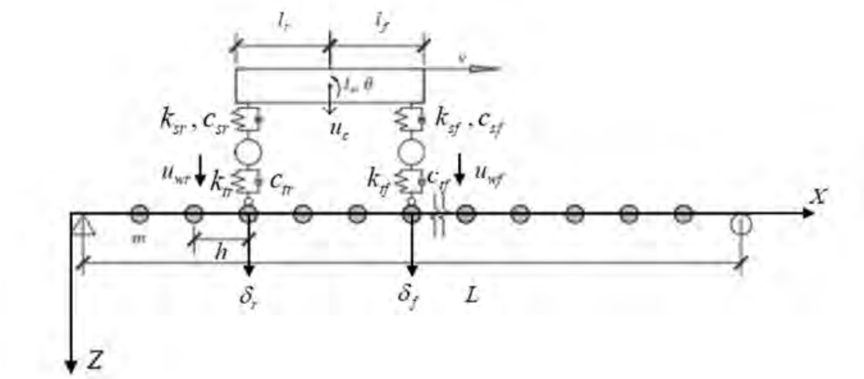

Figure 2.17: 4-DOF vehicle representation

The generalized equation of motion for the vehicle model is obtained.

$$\begin{bmatrix} \boldsymbol{M}_c & \boldsymbol{0} \\ \boldsymbol{0} & \boldsymbol{M}_w \end{bmatrix}\begin{bmatrix} \ddot{u}_c \\ \ddot{u}_w \end{bmatrix}+\begin{bmatrix} \boldsymbol{C}_c & \boldsymbol{C}_{cw} \\ \boldsymbol{C}_{wc} & \boldsymbol{C}_w \end{bmatrix}\begin{bmatrix} \dot{u}_c \\ \dot{u}_w \end{bmatrix}+\begin{bmatrix} \boldsymbol{K}_c & \boldsymbol{K}_{cw} \\ \boldsymbol{K}_{wc} & \boldsymbol{K}_w \end{bmatrix}\begin{bmatrix} u_c \\ u_w \end{bmatrix}=\begin{bmatrix} \boldsymbol{F}_c \\ \boldsymbol{F}_w \end{bmatrix} \qquad [2.93]$$

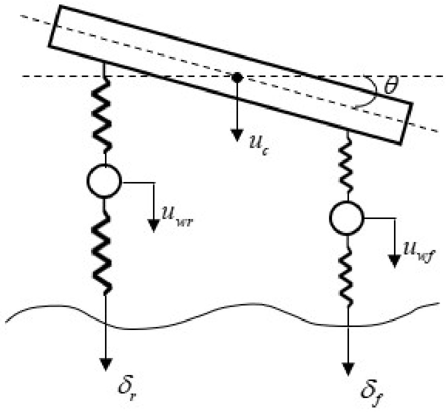

Figure 2.18: Free body diagram of the 4-DOF system

The wheelbase of the car is $l = l_f + l_r$, where l_f and l_r is the distance of the front and rear axle to the center of mass. The spring stiffness is signified as k_{sf} and k_{sr} for front and rear suspension, while the damping coefficients are c_{sf} and c_{sr} sequentially. Accordingly, the tire stiffness and damping are determined by k_{wf} and k_{wr}, c_{wf} and c_{wr}. Also, road irregularities have been taken into consideration as $r(x)$ [section 2.5] describes the roughness of bridge's surface.

The free body diagrams of the car body and the wheels follow.

Car body pitch:

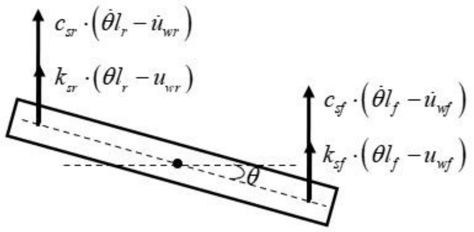

Figure 2.19: Free body diagram of car body in pitch motion

$$-I_c\ddot{\theta} = k_{sf}(\theta \cdot l_f - u_{wf})l_f + k_{sr}(\theta \cdot l_r - u_{wr})l_r + c_{sf}(\dot{\theta} \cdot l_f - \dot{u}_{wf})l_f + c_{sr}(\dot{\theta} \cdot l_r - \dot{u}_{wr})l_r$$

$$I_c\ddot{\theta} + \left(c_{sf}l_f^{\,2} + c_{sr}l_r^{\,2}\right)\dot{\theta} + \left(k_{sf}l_f^{\,2} + k_{sr}l_r^{\,2}\right)\theta - c_{sf}l_f\dot{u}_{wf} + c_{sr}l_r\dot{u}_{wr} - k_{sf}l_f\dot{u}_{wf} + k_{sr}l_r\dot{u}_{wr} = 0 \qquad [2.94]$$

Car body heave:

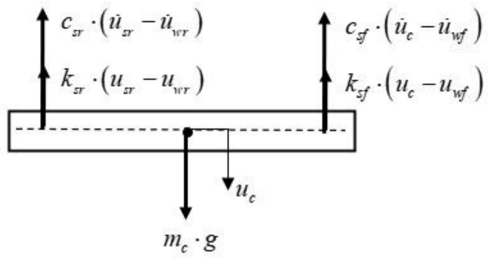

Figure 2.20: Free body diagram of car body in heave motion

$$m_c\ddot{u}_c = -k_{sf}\left(u_c - u_{wf}\right) - k_{sr}\left(u_c - u_{wr}\right) - c_{sf}\left(\dot{u}_c - \dot{u}_{wf}\right) - c_{sr}\left(\dot{u}_c - \dot{u}_{wr}\right) + m_c g$$

$$m_c\ddot{u}_c + \left(c_{sf} + c_{sr}\right)\dot{u}_c + \left(k_{sf} + k_{sr}\right)u_c - c_{sf}\dot{u}_{wf} - k_{sf}u_{wf} - c_{sr}\dot{u}_{wr} - k_{sr}u_{wr} = m_c g \qquad [2.95]$$

Wheel front:

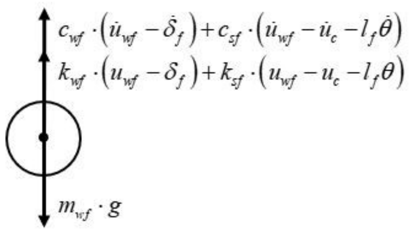

Figure 2.21: Free body diagram of front wheel

$$m_{wf}\ddot{u}_{wf} = -k_{sf}\left(u_{wf} - u_c - l_f\theta\right) + k_{wf}\left(u_{wf} - \left(\delta - r_f\right)\right) - c_{sf}\left(\dot{u}_{wf} - \dot{u}_c - l_f\dot{\theta}\right) + c_{wf}\left(\dot{u}_{wf} - \dot{\delta}\right) + m_{wf}g$$

$$m_{wf}\ddot{u}_{wf} + \left(c_{sf} + c_{wf}\right)\dot{u}_{wf} + \left(k_{sf} + k_{wf}\right)u_{wf} - c_{sf}\dot{u}_c - k_{sf}u_c - c_{sf}l_f\dot{\theta} - k_{sf}l_f\theta = c_{wf}\dot{\delta} + k_{wf}\left(\delta - r_f\right) + m_{wf}g \qquad [2.96]$$

Wheel rear:

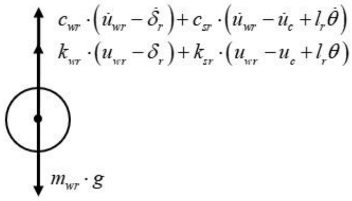

Figure 2.22: Free body diagram of rear wheel

$$m_{wr}\ddot{u}_{wr}=-k_{sr}\left(u_{wr}-u_c+l_r\theta\right)-k_{wr}\left(u_{wr}-\left(\delta-r_r\right)\right)-k_{sr}\left(\dot{u}_{wr}-\dot{u}_c-l_r\dot{\theta}\right)-c_{wr}\left(\dot{u}_{wr}-\dot{\delta}\right)+m_{wr}g$$

$$m_{wr}\ddot{u}_{wr}+\left(c_{sr}+c_{wr}\right)\dot{u}_{wr}+\left(k_{sr}+k_{wr}\right)u_{wr}-c_{sr}\dot{u}_c-k_{sr}u_c+c_{sr}l_r\dot{\theta}+k_{sr}l_r\theta=c_{wr}\dot{\delta}+k_{wr}\left(\delta-r_r\right)+m_{wr}g \quad [2.97]$$

The combined EOM for the whole vehicle assembly is written below.

$$\boldsymbol{M}_v\left\{\ddot{\boldsymbol{u}}_v(t)\right\}+\boldsymbol{C}_v\left\{\dot{\boldsymbol{u}}_v(t)\right\}+\boldsymbol{K}_v\left\{\boldsymbol{u}_v(t)\right\}=\left\{\boldsymbol{F}_v(t)\right\} \quad [2.98]$$

Where,

$$\boldsymbol{M}_v=\begin{bmatrix} m_c & 0 & 0 & 0 \\ 0 & I_c & 0 & 0 \\ 0 & 0 & m_{wf} & 0 \\ 0 & 0 & 0 & m_{wr} \end{bmatrix} \quad [2.99]$$

$$\boldsymbol{K}_v=\begin{bmatrix} k_{sf}+k_{sr} & 0 & -k_{sf} & -k_{sr} \\ 0 & k_{sf}l_f^{\,2}+k_{sr}l_r^{\,2} & -k_{sf}l_f & k_{sr}l_r \\ -k_{sf} & -k_{sf}l_f & k_{sf}+k_{wf} & 0 \\ -k_{sr} & k_{sr}l_r & 0 & k_{sr}+k_{wr} \end{bmatrix} \quad [2.100]$$

$$\boldsymbol{C}_v=\begin{bmatrix} c_{sf}+c_{sr} & 0 & -c_{sf} & -c_{sr} \\ 0 & c_{sf}l_f^{\,2}+c_{sr}l_r^{\,2} & -c_{sf}l_f & c_{sr}l_r \\ -c_{sf} & -c_{sf}l_f & c_{sf}+k_{wf} & 0 \\ -c_{sr} & c_{sr}l_r & 0 & c_{sr}+c_{wr} \end{bmatrix} \quad [2.101]$$

$$\left\{\boldsymbol{F}_v\right\}=\begin{bmatrix} m_c\cdot g \\ 0 \\ m_{wf}\cdot g+c_{wf}\cdot\dot{\delta}+k_{wf}\cdot\left(\delta-r_f\right) \\ m_{wr}\cdot g+c_{wr}\cdot\dot{\delta}+k_{wr}\cdot\left(\delta-r_r\right) \end{bmatrix} \quad [2.102]$$

2.4 External loads on bridge subsystem

The bridge is subjected under each own weight, uniformly distributed over the nodes and the external excitation from the vehicle.

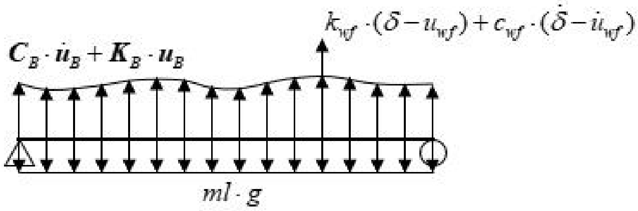

Figure 2.23: External loads on the bridge system

In each step the wheels contact the beam at any point inside the grid and not only on the nodes. The points of contact between the tires and the bridge are calculated as $x_f(t) = v \cdot t$ and $x_r(t) = x_f(t) - l$. Using the transformation from equation [2.67], ξ_a is defined. Assuming that the deformation of the beam between two nodes u_i and u_{i+1} varies linearly, the exact displacement of the bridge δ at the point of contact is calculated via interpolation.

$$\{\boldsymbol{u}_B\} = [\dots \quad \dots \quad u_i \quad \theta_i \quad u_{i+1} \quad \theta_{i+1} \quad \dots \quad \dots]^T$$

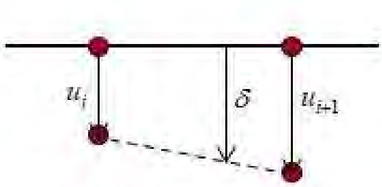

Figure 2.24: Displacement of the bridge at the exact load position

Therefore, the external loads on the bridge are,

$$Q_f = c_{wf}(\dot{u}_{wf} - \dot{\delta}_f) + k_{wf}(u_{wf} - \delta_f) \qquad [2.103]$$

$$Q_r = c_{wr}(\dot{u}_{wr} - \dot{\delta}_r) + k_{wr}(u_{wr} - \delta_r) \qquad [2.104]$$

and they establish the local force vectors for front and rear, according to the equation [2.83].

The equation of motion for the bridge subsystem as described in the section [2.2.2] is,

$$\boldsymbol{M}_B \cdot \{\ddot{\boldsymbol{u}}_B\} + \boldsymbol{C}_B \cdot \{\dot{\boldsymbol{u}}_B\} + \boldsymbol{K}_B \cdot \{\boldsymbol{u}_B\} = \{\boldsymbol{F}_B(t)\} \quad [2.105]$$

where the external force vector $\{\boldsymbol{F_B(t)}\}$ contains the distributed weight, and the two local force vectors $\boldsymbol{F^e}$ which are implemented by superposition.

2.5 Road irregularities

To simulate the road irregularities, ISO 8608 is used to standardize the road profile as it is measured by the Power Spectral Density (PSD) of its vertical displacement (G_d) [3, 8 - 10, 12]. PSD explains how the amplitude of the irregularities varies with the frequency ($n = \Omega/2\pi$ cycles/m) and angular frequency (Ω rad/m). Hence the displacement PSD can be either function of n as $G_d(n)$ or function of Ω as $G_d(\Omega)$.

The PSD is formulated as,

$$G_d(n) = G_d(n_0) \cdot \left(\frac{n}{n_0} \right)^{-w}$$

$$G_d(\Omega) = G_d(\Omega_0) \cdot \left(\frac{\Omega}{\Omega_0} \right)^{-w}$$

Where,

- $n_0 = 0.01$ cycles/m is the reference frequency.
- $\Omega_0 = 1$ rad/m is the reference angular frequency.
- $w = 2$ is the exponent of the fitted PSD.
- $G_d(n_0)$ and $G_d(\Omega_0)$ can be located in the table below.

Table 2.1: ISO 8608 values of $G_d(n_0)$ *and* $G_d(\Omega_0)$

Road Class	$G_d(n_0)\,(10^{-6} m^3)$		$G_d(\Omega_0)\,(10^{-6} m^3)$	
	Lower limit	Upper limit	Lower limit	Upper limit
A	-	32	-	2
B	32	128	2	8
C	128	512	8	32
D	512	2048	32	128
E	2048	8192	128	512
F	8192	32768	512	2048
G	32768	131072	2048	8192
H	131072	-	8192	-
	$n_0 = 0.1\, cycles/m$		$\Omega_0 = 1\, rad/m$	

Road roughness is a stochastic representation of the function of Power Spectral Density of vertical displacements. For a road profile with length L and for specific frequency n equally spaced along the length, as $\Delta n = 1/L$, the value of PSD is given by the mean square value of the signal (Ψ_x) as,

$$G_d(n) = \lim_{\Delta n \to 0} \cdot \frac{\Psi_x^{\,2}}{\Delta n} \qquad [2.106]$$

The profile signal then it is considered as a uniform sequence of points spaced equally along the length of the road.

$$G_d(n) = \frac{\Psi_x^{\,2}(n_i, \Delta n)}{\Delta n} \qquad , \; i \in \left[0, N = \frac{n_{\max}}{\Delta n}\right] \qquad [2.107]$$

Where n_{max} is the maximum sampling frequency and n_i is each discretized frequency equidistant Δn.

Their random displacement of road surface can be described by the harmonic function.

$$h(x) = A_i \cdot \cos\left(2\pi \cdot n_i \cdot x + \varphi_i\right) \qquad [2.108]$$

Where,

- A_i is the amplitude of the roughness.
- The phase angle φ_i takes random values of normal distribution between 0 and 2π.
- N is the number of discrete frequency segments.

It can be considered that, the mean square value of the harmonic signal is defined through the amplitude as,

$$\Psi_x^2 = \frac{A_i^2}{2} \quad [2.109]$$

The PSD value now is equal to,

$$G_d(n_i) = \frac{A_i^2}{2 \cdot \Delta n} \quad [2.110]$$

A custom road profile along the whole length of the road is produced by,

$$h(x) = \sum_{i=0}^{N} A_i \cdot \cos\left(2\pi \cdot n_i \cdot x + \varphi_i\right)$$

$$h(x) = \sum_{i=0}^{N} \sqrt{2 \cdot \Delta n \cdot G_d(n_i)} \cdot \cos\left(2\pi \cdot n_i \cdot x + \varphi_i\right)$$

$$h(x) = \sum_{i=0}^{N} \sqrt{\Delta n} \cdot 2^k \cdot 10^{-3} \cdot \frac{n_0}{n_i} \cdot \cos\left(2\pi \cdot n_i \cdot x + \varphi_i\right) \quad [2.111]$$

Where,

- $n_i = i \cdot \Delta n$
- $\Delta n = \frac{1}{L}$
- $n_{max} = \frac{1}{B}$
- $N = \frac{n_{max}}{\Delta n} = \frac{L}{B}$
- k is a constant defined through ISO classification in the table below.
- $n_0 = 0.1$ cycles/m
- $\varphi_i \in [0,2\pi]$ random phase angle

Table 2.2: k values for ISO road irregularities classification

Road Class		k
Upper limit	Lower limit	
A	B	3
B	C	4
C	D	5
D	E	6
E	F	7
F	G	8
G	H	9

It should be noticed that a road profile with discrete irregularities such as curbs, joints, potholes or cracking zones cannot be described by the Power Spectral Density method.

2.6 Coupled system

The combined EOM for the coupled vehicle and bridge system is represented below.

$$\boldsymbol{M}\,\{\ddot{\boldsymbol{u}}\} + \boldsymbol{C}\,\{\dot{\boldsymbol{u}}\} + \boldsymbol{K}\,\{\boldsymbol{u}\} = \{\boldsymbol{F}(t)\} \qquad [2.112]$$

Where $\{\boldsymbol{u}\} = \begin{bmatrix}\boldsymbol{u}_v & \boldsymbol{u}_w & \boldsymbol{u}_B\end{bmatrix}^T \in \mathbf{R}^{(2N+4)x1}$ is the displacement vector of the coupled system.

The $\boldsymbol{M}$, $\boldsymbol{C}$ and $\boldsymbol{K} \in \mathbf{R}^{(2N+4)x(2N+4)}$ are the mass, damping and stiffness matrices and $\{\boldsymbol{F}(t)\} \in \mathbf{R}^{(2N+4)x1}$ is the forces vector.

$$\boldsymbol{M} = \begin{bmatrix}\boldsymbol{M_v} & \boldsymbol{0} \\ \boldsymbol{0} & \boldsymbol{M_B}\end{bmatrix} \qquad [2.113]$$

$$\boldsymbol{K} = \begin{bmatrix}\boldsymbol{K_v} & \boldsymbol{0} \\ \boldsymbol{0} & \boldsymbol{K_B}\end{bmatrix} \qquad [2.114]$$

$$\boldsymbol{C} = \begin{bmatrix}\boldsymbol{C_v} & \boldsymbol{0} \\ \boldsymbol{0} & \boldsymbol{C_B}\end{bmatrix} \qquad [2.115]$$

$$\{\boldsymbol{F}(t)\} = \begin{bmatrix}\{\boldsymbol{F}_v(t)\} \\ \{\boldsymbol{F}_B(t)\}\end{bmatrix} \qquad [2.116]$$

The coupled system of the vehicle and bridge is solved as a second order differential equation with the Newmark's – β method.

2.7 Solution: Newmark's - β method

Since the matrices $\boldsymbol{M}$, $\boldsymbol{C}$ and $\boldsymbol{K}$ are constant and $\{\boldsymbol{F}(t)\}$ is a function only of time, the equations are linear differential and hence the solution can be approached by Newmark's - β method [4, 13]. This method implements the mean value theorem for the displacement vector $\{\boldsymbol{u}(\boldsymbol{t})\}$ and there is a constant variable β so that,

$$u(t+\Delta t) - u(t) = u'(t+\beta\Delta t)\cdot\Delta t \qquad [2.117]$$

By the use of Taylor's series up to 3rd order derivative of u and by applying the generalized mean value theorem, the derivatives are,

$$\boldsymbol{u}''_{n+1} = \frac{\boldsymbol{u}_{n+1} - \boldsymbol{u}_n}{\beta \Delta t^2} - \frac{\boldsymbol{u}'_n}{\beta \Delta t^2} - \left(\frac{1}{2\beta} - 1 \right) \boldsymbol{u}''_n \qquad [2.118]$$

And

$$\boldsymbol{u}'_{n+1} = \frac{\gamma \left(\boldsymbol{u}_{n+1} - \boldsymbol{u}_n \right)}{\beta \Delta t} + \boldsymbol{u}'_n \frac{1-\gamma}{\beta} + \Delta t \boldsymbol{u}''_n \left(\frac{1-\gamma}{2\beta} \right) \qquad [2.119]$$

A change in β affects the variation in acceleration over the given time interval. Coefficient γ illustrates the property of numerical artificial damping introduced by discretization in time domain.

The method is unconditionally stable for $\gamma \geq 0.5$ and $\beta \geq 0.25(0.5+\gamma)^2$ and conditionally stale for $\gamma \geq 0.5$. For the purpose of this study $\beta = 0.25$ and $\gamma = 0.5$ were used.

This method is based at the assumption that at each time step t the displacement of the next timestep $t+1$ is calculated as below.

$$\boldsymbol{A} \cdot \boldsymbol{u}_{n+1} = \boldsymbol{B}_n \qquad [2.120]$$

Where,

$$\boldsymbol{A} = \frac{\boldsymbol{M}}{\beta \Delta t^2} + \frac{\gamma \boldsymbol{C}}{\beta \Delta t} + \boldsymbol{K} \qquad [2.121]$$

$$\boldsymbol{B}_n = \boldsymbol{f}(t_n + 1) + \boldsymbol{M}\left[\frac{\boldsymbol{u}_n}{\beta \Delta t^2} + \frac{\boldsymbol{u}'_n}{\beta \Delta t} + \left(\frac{1}{2\beta} - 1 \right) \boldsymbol{u}''_n \right] + \boldsymbol{C}\left[\frac{\gamma \boldsymbol{u}_n}{\beta \Delta t} - \boldsymbol{u}'_n \frac{1-\gamma}{\beta} - \Delta t \boldsymbol{u}''_n \left(1 - \frac{\gamma}{2\beta} \right) \right] \qquad [2.122]$$

2.8 Results

Below are the results for the simply supported beam bridge and the vehicle in its two cases: a) simplified 1 - wheel vehicle and b) 2 - wheel vehicle. The inputs are used for the presented results are depicted in the following table.

Table 2.3: Vehicle bridge interaction inputs

Bridge parameters	1 – wheel vehicle parameters	2 – wheel vehicle parameters
$L = 30\,m$	$m_c = 17735\,kg$	$m_c = 17735\,kg$
$EI = 2.5\times10^{12}\ N\cdot m^2$	$k_c = 6\times10^6\ N/m$	$I_c = 1.47\cdot10^5\ kg\cdot m^2$
$\rho A = 5\times10^3\ kg/m$	$c_c = 7\times10^4\ N\cdot s/m$	$k_{sf} = 2.47\times10^6\ N/m$
	$m_w = 3000\,kg$	$k_{sr} = 4.23\times10^6\ N/m$
	$k_w = 8\times10^6\ N/m$	$c_{sf} = 3\times10^4\ N\cdot s/m$
	$c_w = 8\times10^3\ N/m$	$c_{sr} = 4\times10^4\ N\cdot s/m$
		$m_w = 1500\,kg$
		$k_w = 4\times10^6\ N/m$
		$c_w = 4\times10^3\ N/m$
		$l = 3.3\,m$
		$weight\ bias = 40\,\%\ front$

The simulations were run for road profile classifications A, B and C from the irregularities table.

Table 2.4: Road profile classes used for the simulations

Road Class	$G_d(n_0)\,(10^{-6}m^3)$		$G_d(\Omega_0)\,(10^{-6}m^3)$	
	Lower limit	Upper limit	Lower limit	Upper limit
A	-	32	-	2
B	32	128	2	8
C	128	512	8	32
	$n_0 = 0.1\,cycles/m$		$\Omega_0 = 1\,rad/m$	

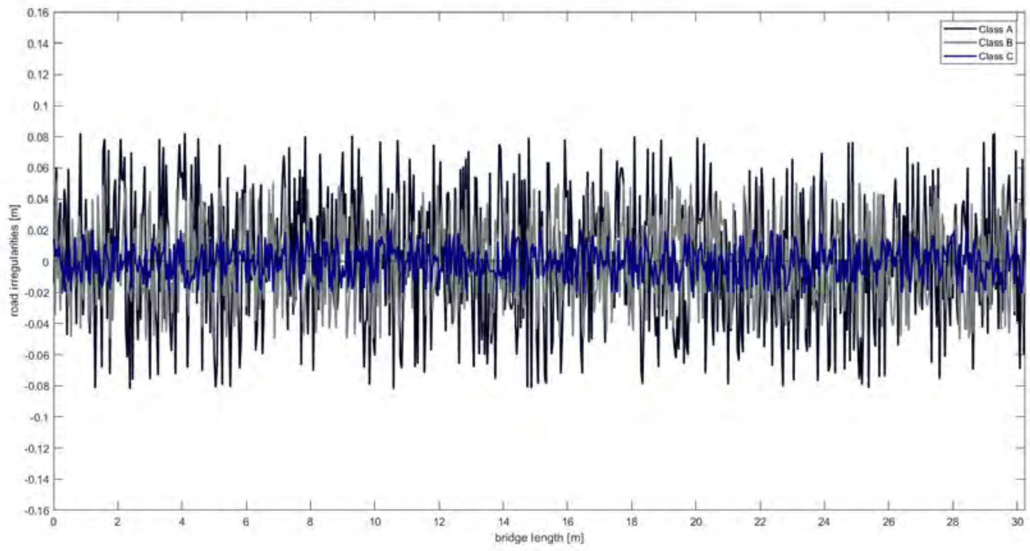

Figure 2.25: Road irregularities profiles over the span of the bridge

While the vehicle passes over the bridge length at constant velocity $v = 100\ kph$, both vehicle and bridge are subjected to excitations as the figures [2.26 – 2.32] indicate.

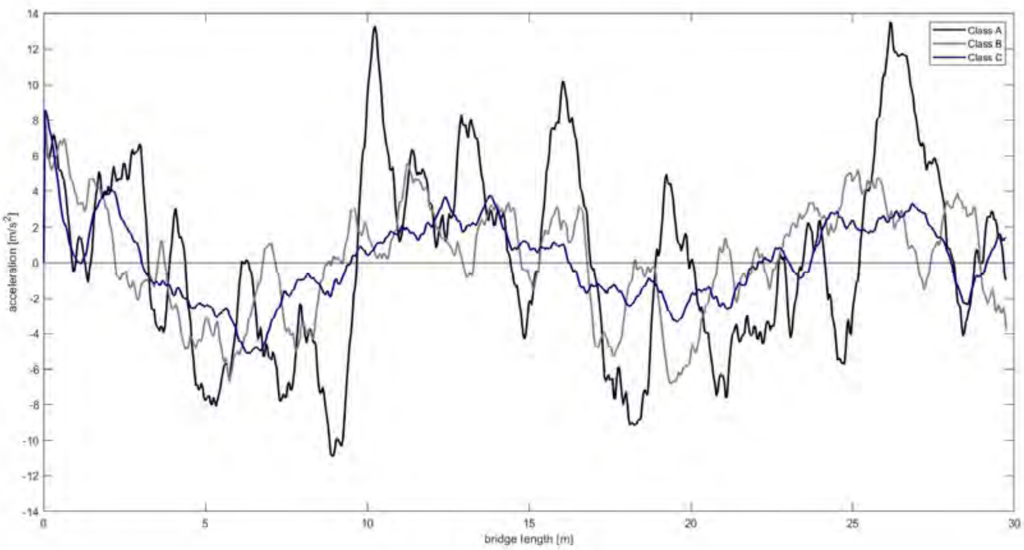

Figure 2.26: Car body vertical acceleration of 1 - wheel vehicle for Class A, B, C roughness

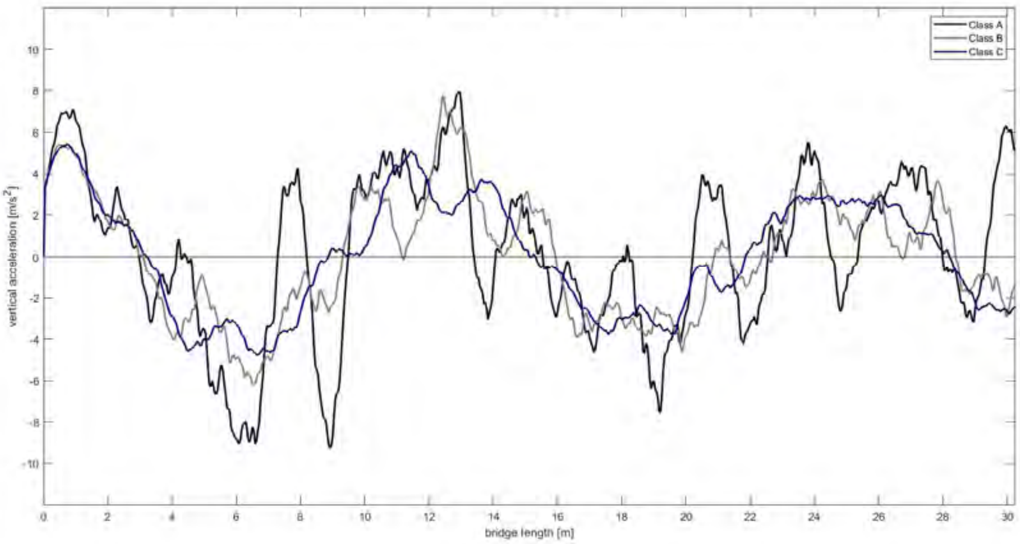

Figure 2.27: Car body vertical acceleration of 2 - wheel vehicle for Class A, B, C roughness

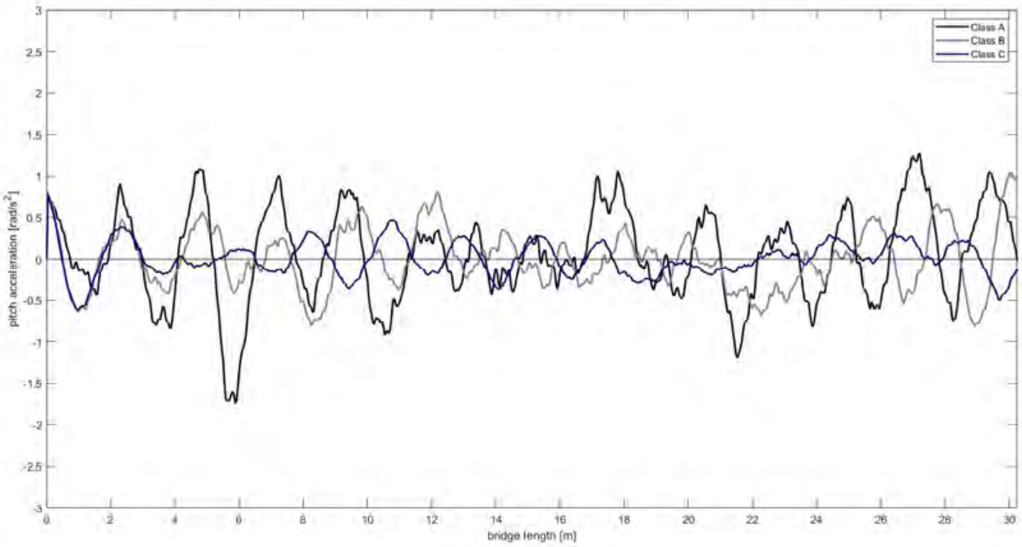

Figure 2.28: Car body pitch acceleration of 2 - wheel vehicle for Class A, B, C roughness

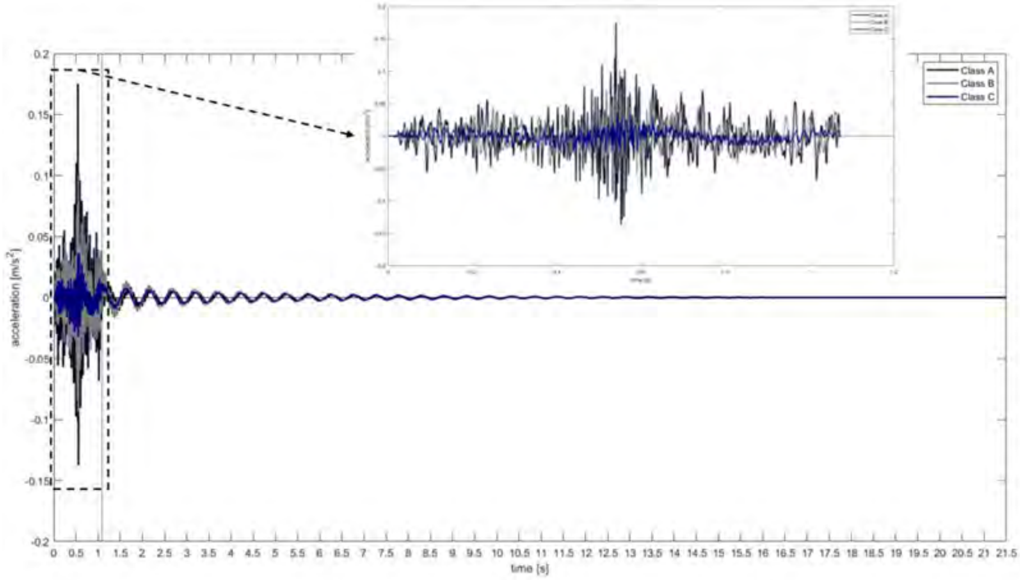

Figure 2.29: Midpoint acceleration of bridge for a 1 - wheel vehicle for Class A, B, C roughness

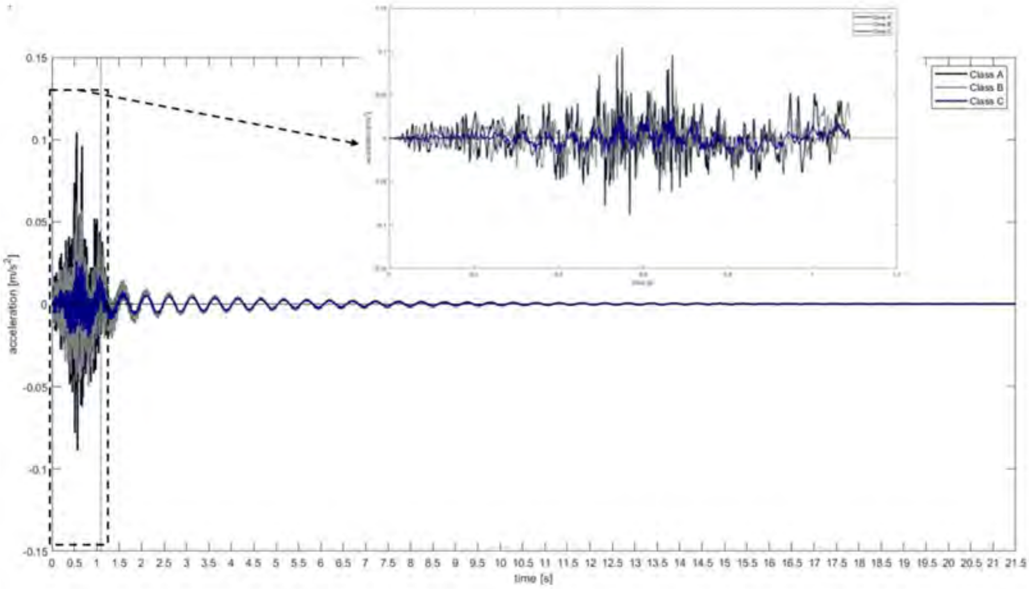

Figure 2.30: Midpoint acceleration of bridge for a 2 - wheel vehicle for Class A, B, C roughness

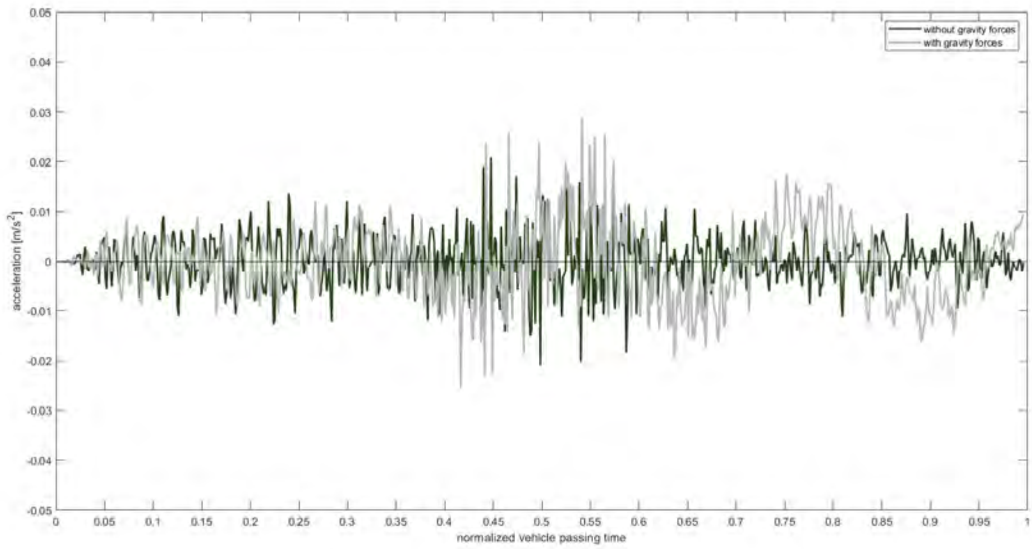

Figure 2.31: Car body acceleration for a 2 – wheel vehicle over class C irregularities – effect of gravity forces

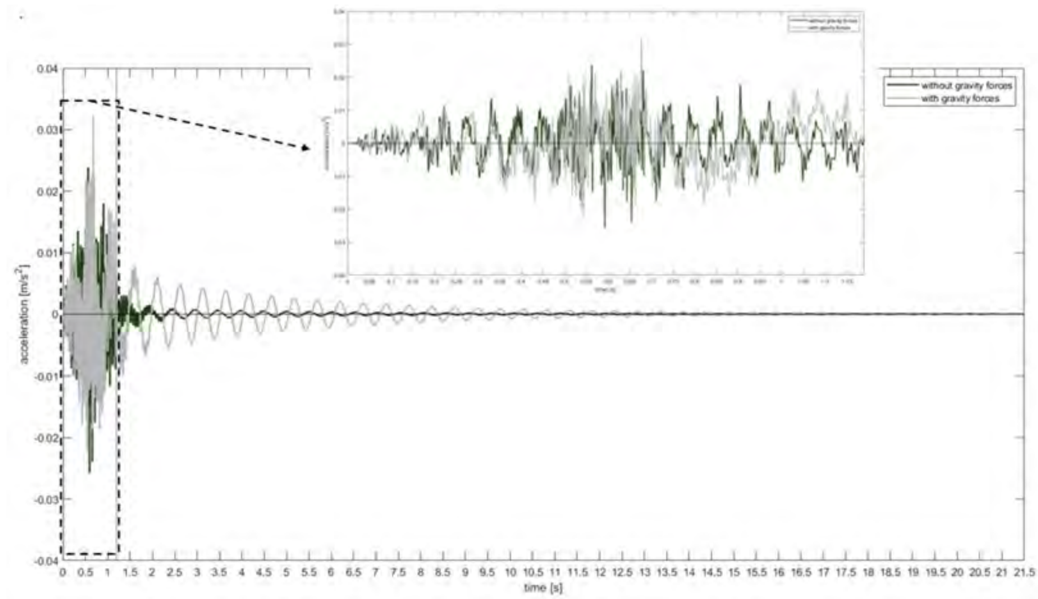

Figure 2.32: Midpoint acceleration over class C irregularities for 2 – wheel vehicle – effect of gravity forces

The variation of EI affects the overall stiffness of the bridge. The displacement of midpoint is represented in the next diagrams, for a 2 – wheel vehicle at speed $v = 100\,kph$ and a road profile of class C.

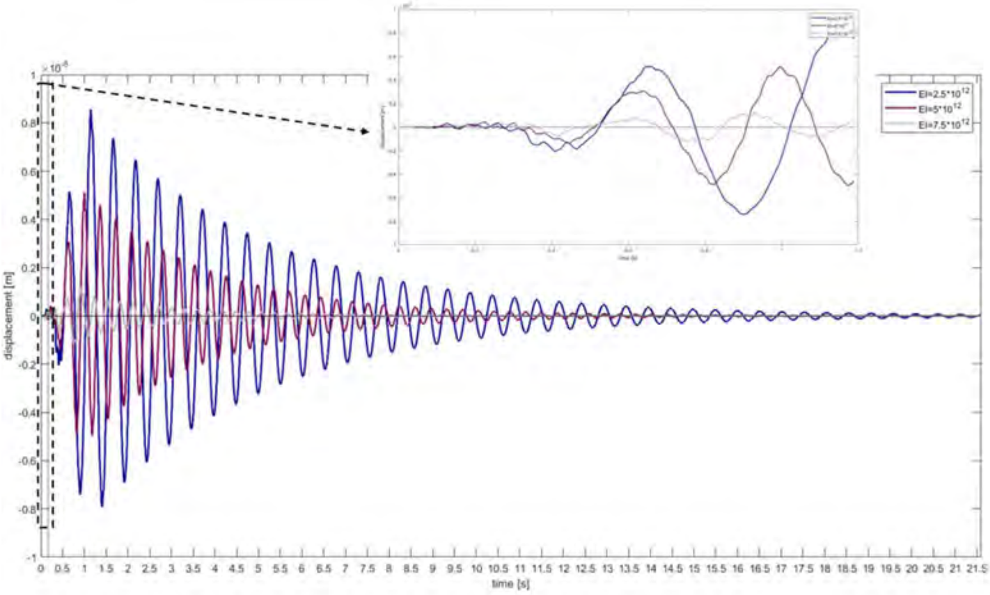

Figure 2.33: Midpoint displacement over time for various EI – without gravity forces

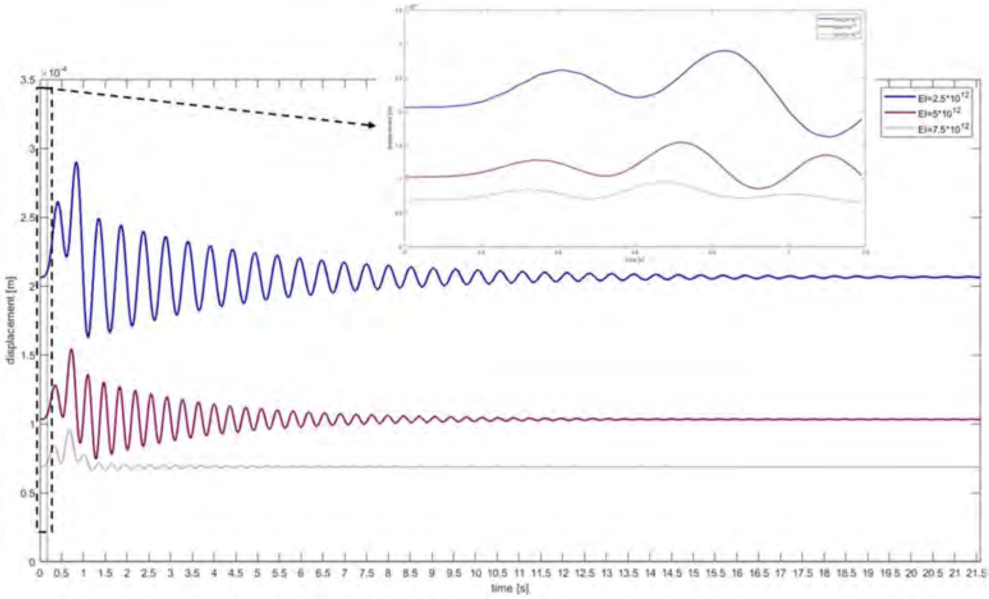

Figure 2.34: Midpoint displacement over time for various EI – with gravity forces

The variation of vehicle speed affects the overall response of the bridge. The acceleration of midpoint is represented in the next diagrams, for a 2 – wheel and a road profile of class C.

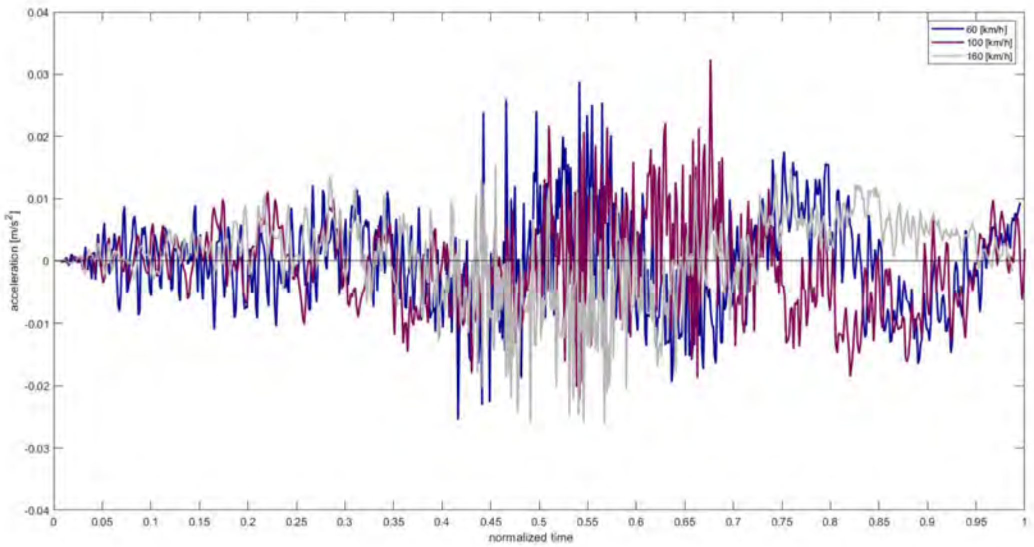

Figure 2.35: Midpoint acceleration for class C irregularities – without gravity forces

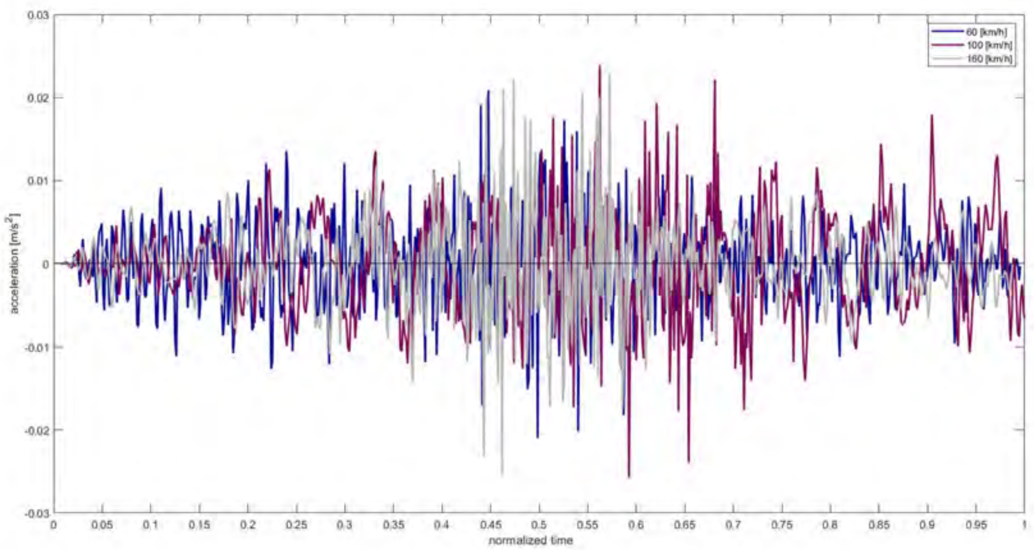

Figure 2.36: Midpoint acceleration for class C irregularities – with gravity forces

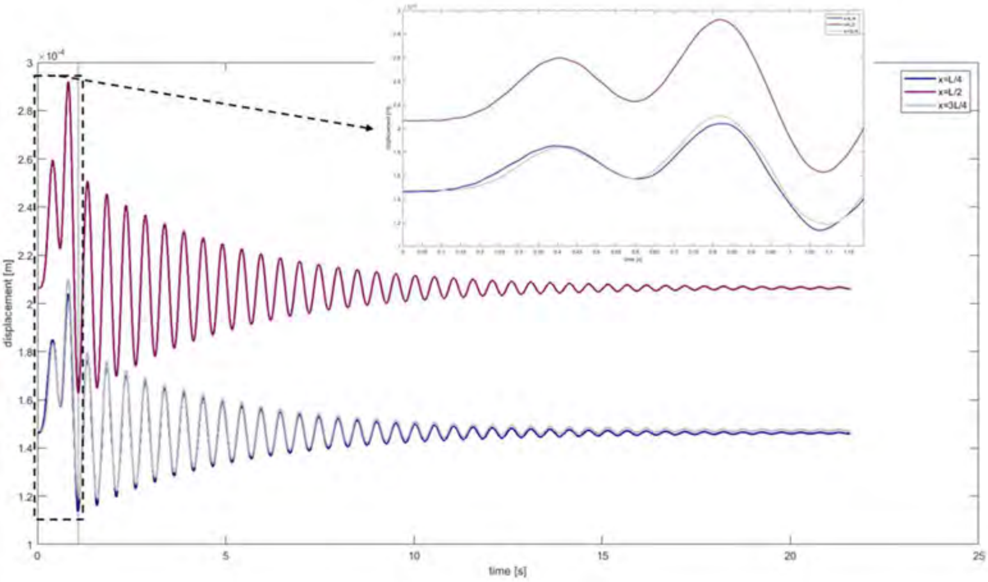

Figure 2.37: Bridge displacement at L/4, L/2, 3L/4 – zoom at the time period when the car is on the bridge

The comparison of these two cases reveals similarities in both the response of their bodies and the bridge. Both vehicles have the same masses, while the spring-damper values of the single wheel are equal to the 2-wheel vehicle, assuming they act in parallel. The relatively small wheelbase of the second vehicle compared to the length of the bridge is probably responsible for their resembling behavior. The following graphs focus on these common characteristics as the two vehicles move at a speed of 100 kph over irregularities of class C.

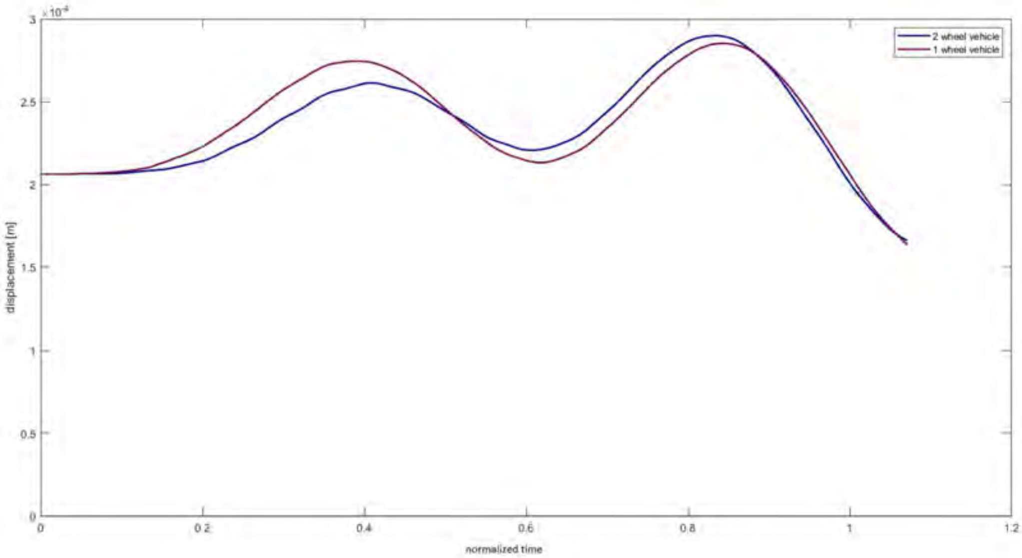

Figure 2.38: Midpoint displacement under 1 – wheel vs 2 – wheel passing vehicle

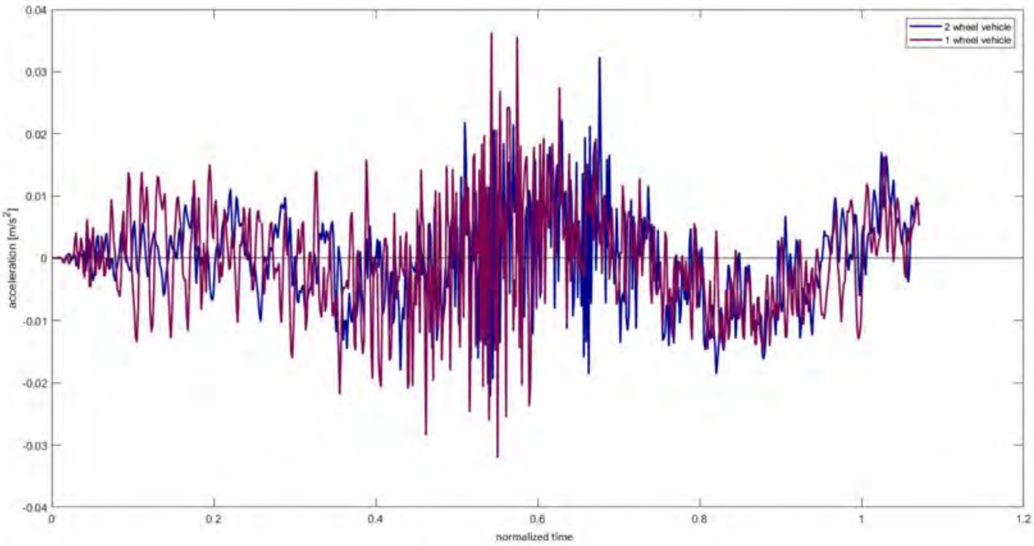

Figure 2.39: Midpoint acceleration under 1 – wheel vs 2 – wheel passing vehicle

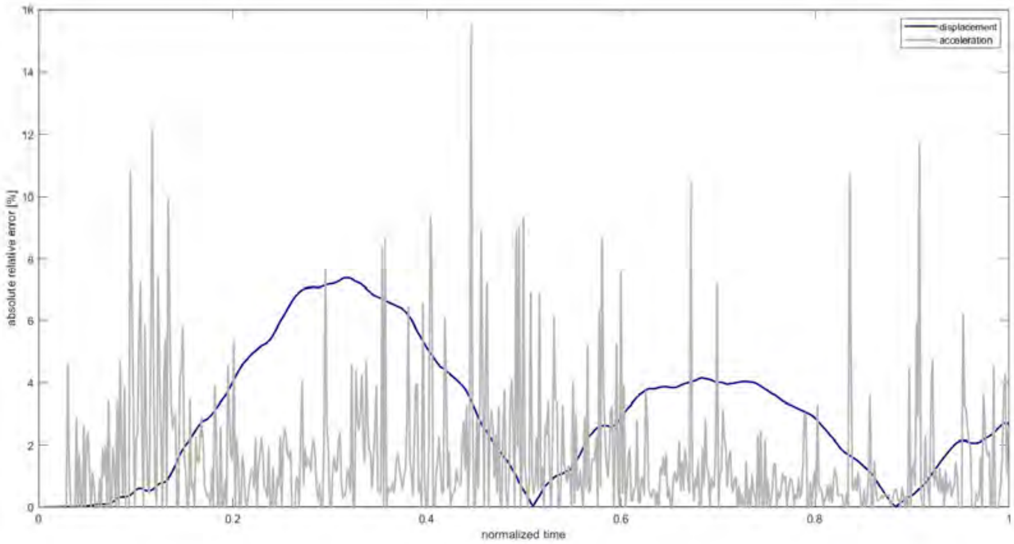

Figure 2.40: Absolute relative error between 1 – wheel and 2 – wheel passing vehicle

Chapter 3

Effect of suspension design characteristics on vehicle's loads

3.1 Introduction

The following chapter aims to analyze the response of a vehicle as it is simulated over different road profiles. In these scenarios the detail of the vehicle is the key factor for its response. The vehicle is a single seater formula student race car, consisting by its original components and simulated containing all the geometric and material properties.

The object is a car running on a straight rigid road with various categories of road qualities. The methodology for creating the road roughness is the Power Spectral Density which was analyzed in section 2.5 of the previous chapter. As the vehicle interacts with the pavement, forces and moments are developed at the tire's contact patch at all dimensions. The tire's behavior is critical, since it is simulated as deformable component contributes to the transmissibility of the external load to the rest of the vehicle. The analysis of the suspension that takes place includes key characteristics for the dynamic response of the vehicle. There is a breakdown in the springs and dampers selection, taking into account the desired damping frequencies. The distinctive feature of this vehicle is the suspension system that it uses. Double unequal wishbone decoupled system. Which alters the calculations methodology against the conventional one.

The generation of the multi-body model was done in Altair MotionView [34 – 36]. Each component was extracted from CAD software and then imported and connected on the vehicle assembly.

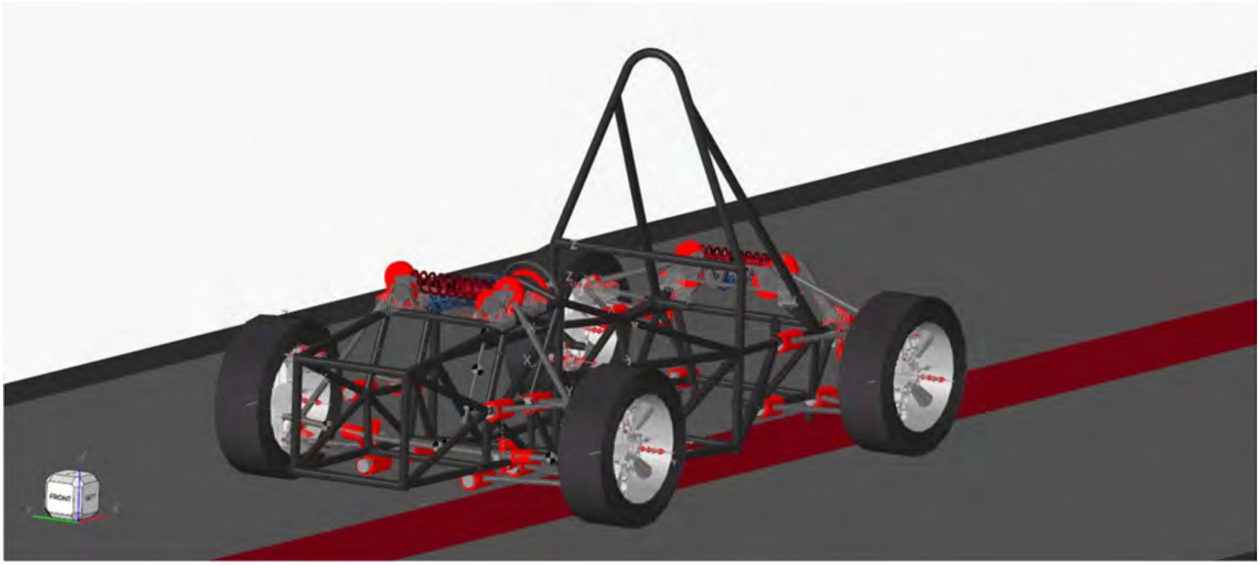

Figure 3.1: Formula student vehicle

3.2 Suspension characteristics

Fundamental suspension characteristics which are used for the analysis of the vehicle are explained in this sector [24, 29].

3.2.1 Motion ratio

The motion ratio of suspension system is a measure that relates the wheel center displacement with the spring displacement. It is used to calculate the amount of spring's deflection under a specific load applied on the wheel center. According to the documentation, motion ratio value is aimed to be as close to 1 as possible. It is defined as,

$$MR = \frac{wheel\ displacement}{spring\ displacement} = \frac{\delta_w}{\delta_s} \qquad [3.1]$$

3.2.2 Wheel rate

Wheel rate is the effective spring rate when it is measured at the wheel center. It helps with the mathematical analysis of the suspension system and combines the ride frequencies of the car to the desired spring stiffness.

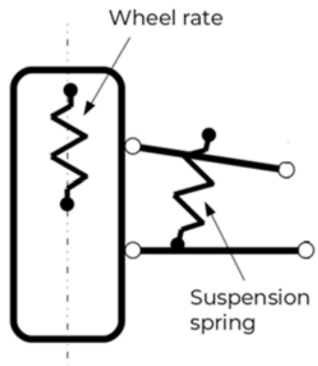

Figure 3.2: Wheel rate representation

Energy equation on wheel – spring systems can be applied.

$$F_w \cdot \delta_w = F_s \cdot \delta_s \Rightarrow MR = \frac{F_s}{F_w} \qquad [3.2]$$

$$F_w \cdot \delta_w = F_s \cdot \delta_s$$

$$WR \cdot \delta_w^{\ 2} = SR \cdot \delta_s^{\ 2}$$

$$WR = \frac{SR}{MR^2} \qquad [3.3]$$

Introducing wheel rate definition, any complex suspension system can be converted to the simplified one below.

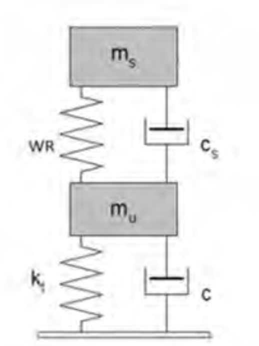

Figure 3.3: Simplified suspension system of quarter car model

Here, k_t and c_t is the tire's stiffness and damping, while m_s is the vehicle's suspended mass and m_u is the non-suspended mass. As suspended mass is considered to be every part of the vehicle that is supported by the springs, like the engine, chassis, driver etc. In the non-suspended mass belong the rims, tires, wheel hubs etc. In other words, the mass of these components does not affect the springs static deformation. In this paper, there will be instances of separation between the suspended and the total mass of the car. It is important to note that the distribution of the total mass differs from the suspended mass.

3.2.3 Frequency

Two modes of vibration exist. The first concerns the vibration of the sprung mass (m_s) relative to the ground. The two springs are studied as springs in series and combined in a total spring stiffness, called Ride Rate (K_R).

$$\frac{1}{K_R} = \frac{1}{WR} + \frac{1}{K_t} \qquad [3.4]$$

The frequency of vibration of the first mode is calculated next.

$$f_s = \frac{1}{2\pi} \cdot \sqrt{\frac{K_R}{m_s}} \qquad [3.5]$$

The second mode concerns the vibration of the wheels relative to the chassis. The two springs are connected in parallel $(WR + k_t)$.

The frequency of vibration of the second mode is calculated next.

$$f_u = \frac{1}{2\pi} \cdot \sqrt{\frac{WR + K_t}{m_u}} \qquad [3.6]$$

Frequency will be used to select the required springs and dampers for heave/pitch and roll modes of vibration of the whole vehicle.

It is easy to understand that a lower value in frequency leads to a smoother ride but slower response. On the other hand, a higher frequency results in stiffer ride but more difficult to handle. Common values can be found in the documentation and experimental studies.

3.2.4 Damping

Mass, spring stiffness and damping stiffness define two important parameters. The frequency as described above and critical damping coefficient.

The energy flow during a vibration can be described through a transfer function. It is a measure of how efficiently a forcing vibration can produce an excited vibration [6]. In terms of suspension, transmissibility calculates the chassis vertical movement over bumps [28 – 31].

Suppose the oscillation under irregular road profile $h(x)$. The road profile is constant along its length, but since the car is moving the excitation force is a function of time.

$r(t) = h(x(t)) = irregular\ road\ profile = known$

$u(t) = body\ excitation\ in\ relation\ to\ the\ ground$

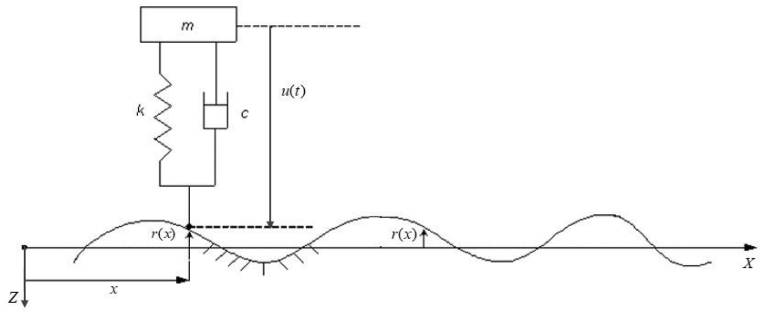

Figure 3.4: Oscillated suspended mass over a road with irregularities

The below free body diagram on the oscillating mass is considered to analyze the response of the presented system.

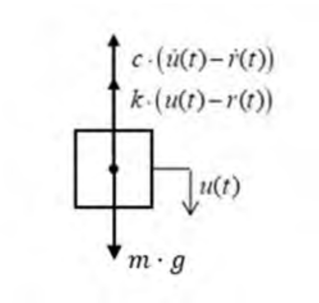

Figure 3.5: Free body diagram of suspended mass

Equation of motion on mass body:

$$m\cdot\ddot{u}(t) = -k\cdot\left(u(t)-r(t)\right)-c\cdot\left(\dot{u}(t)-\dot{r}(t)\right)+m\cdot g$$

$$m\cdot\ddot{u}(t)+c\cdot\dot{u}(t)+k\cdot u(t)=k\cdot r(t)+c\cdot\dot{r}(t)+m\cdot g \quad [3.7]$$

The total external force is $F_{total}(t)=F(t)+mg$ where,

$$F(t)=k\cdot r(t)+c\cdot\dot{r}(t) \quad [3.8]$$

For sinusoidal excitation $r(t)=S_o\cdot\cos(\Omega\cdot t)$ the equation [3.8] is written as follows.

$$F(t) = k \cdot S_o \cdot \cos(\Omega \cdot t) - c \cdot S_o \cdot \Omega \cdot \sin(\Omega \cdot t)$$

$$F(t) = \sqrt{k^2 + (c \cdot \Omega)^2} \cdot S_o \cdot \cos(\Omega \cdot t - \theta)$$

$$F(t) = k \cdot S_o \cdot \sqrt{1 + \left(\frac{c \cdot \Omega}{k}\right)^2} \cdot \cos(\Omega \cdot t - \theta) \qquad [3.9]$$

Where, $\tan\theta = -\frac{c \cdot S_o \cdot \Omega}{k \cdot S_o} = -\frac{c \cdot \Omega}{k} = -2 \cdot \zeta \cdot \eta$

The total response of the system is the superposition of the u_{st} and the response due to the base excitation.

$$u_{total}(t) = u_{st} + u(t) \qquad [3.10]$$

$$u_{st} = \frac{mg}{k} \qquad [3.11]$$

The system is oscillated around u_{st}, at a frequency and amplitude defined by u(t) as,

$$u(t) = X(\eta, \zeta) \cdot \sqrt{1 + (2 \cdot \zeta \cdot \eta)^2} \cdot S_o \cdot \cos(\Omega \cdot t - \theta - \varphi) \qquad [3.12]$$

- $\tan\varphi = \frac{2 \cdot \zeta \cdot \eta}{1 - \eta^2}$
- $X(\eta, \zeta) = \frac{1}{\sqrt{(1-\eta^2)^2 + (2 \cdot \zeta \cdot \eta)^2}}$

The amplification factor for the base forces is formulated as follows.

$$X_R(\eta, \zeta) = X(\eta, \zeta) \cdot \sqrt{1 + (2 \cdot \zeta \cdot \eta)^2}$$

$$X_R(\eta, \zeta) = \frac{\sqrt{1 + (2 \cdot \zeta \cdot \eta)^2}}{\sqrt{(1-\eta^2)^2 + (2 \cdot \zeta \cdot \eta)^2}} \qquad [3.13]$$

- $\eta = \frac{\Omega}{\omega_0}$
- $\omega_0 = 2\pi \cdot f_s$

$X_R(\eta, \zeta)$ is the transmissibility ratio of the vibration since it represents the ratio between the output to the input amplitude of displacement.

$$X_R(\eta,\zeta) = \frac{output}{input} \quad [3.14]$$

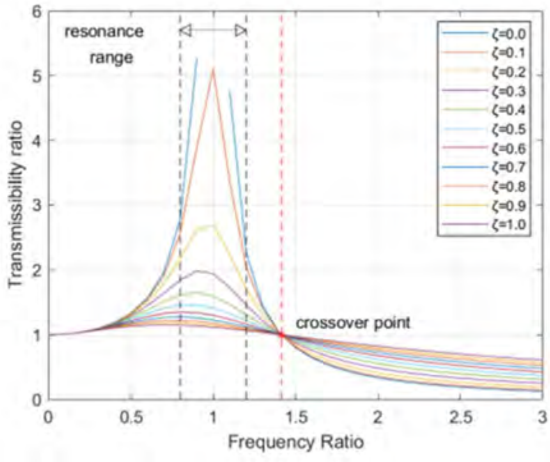

Figure 3.6: Transmissibility ratio for a damping ratio range

- $X_R(\eta,\zeta) = 1$: the car body moves the same as the wheels
- $X_R(\eta,\zeta) > 1$: the car body is oscillated at higher amplitude than the wheels
- $X_R(\eta,\zeta) < 1$: the car body is oscillated at lower amplitude than the wheels.

The desired magnitude of transmissibility ratio is the lowest possible. For low frequencies (left side of crossover point) a higher damping ratio is preferred. On the other hand, higher frequencies are matched with higher damping ratios. At the low range, as the frequency increases approaches a point where the car's body amplitude is maximum. This frequency is called resonant frequency and corresponds to maximum transmissibility. This leads the damping ratio to a range from 0.5 – 0.7.

Critical damping coefficient is,

$$c_{crit} = 2 \cdot \sqrt{k_R \cdot m_s} \quad [3.15]$$

Using equation [3.5], the equation [3.15] is written as,

$$c_{crit} = 4 \cdot \pi \cdot f_s \cdot m_s \quad [3.16]$$

Similarly with springs, the dampers are not directly attached to the wheel center, but they are linked to the corresponding spring. Due to that motion ratio must be imposed and the final formulation of critical damping ratio is quoted below.

$$c_{crit} = 4 \cdot \pi \cdot f_s \cdot m_s \cdot MR^2 \quad [3.17]$$

A damping curve shows the way a damper responds to different speeds. Starting from the standard equation between force and velocity, an initial baseline curve for heave and roll is created.

$$F = c \cdot V$$

$$F = \zeta \cdot c_{crit} \cdot V$$

$$F = \zeta \cdot 4 \cdot \pi \cdot f_s \cdot m_s \cdot MR^2 \cdot V \qquad [3.18]$$

For specific damping ratio and frequency, a linear curve is produced. An example is the following.

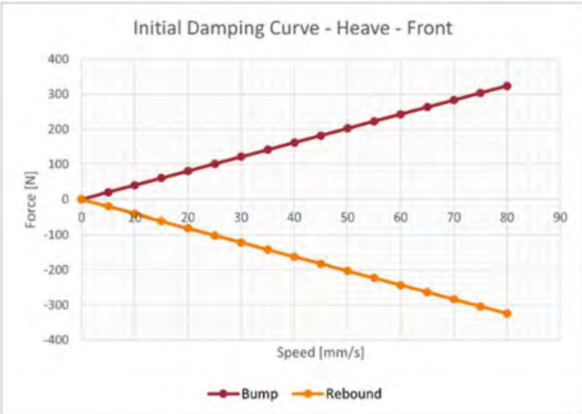

Figure 3.7: Initial damping curve for bump and rebound

The shock absorbers that are used for this study have two settings for bump and two for rebound, one for low speed range and one other for high speed. The corresponding coefficients that are used to adjust the initial curve to the modified one, could be searched in relevant published literature.

Initial curves for both bump and rebound are symmetrical along x axis. Generally, in heave during compression most of the energy is absorbed by the spring so less damping force is required. However, during rebound the released energy needs to be controlled, so more damping force is necessary.

Heave:

$$F_{low\ speed\ compression} = 2/3 \cdot F_0 \qquad [3.19]$$

$$F_{high\ speed\ compression} = 1/3 \cdot F_0 \qquad [3.20]$$

$$F_{low\ speed\ rebound} = 3/2 \cdot F_0 \qquad [3.21]$$

$$F_{high\ speed\ rebound} = 3/4 \cdot F_0 \qquad [3.22]$$

The roll motion is more complex due to its attachment mechanism. The spring - damper is compressed when the chassis rotates outward left or right, while it rebounds to return to its initial position. For simplification reasons, in this paper it is considered that the compression is on the left side and rebound on the right. This direction is affected by the kinematic points on left and right rocker. Hence, roll is symmetric because the compression on the left side corresponds to the rebound on the right and vice versa.

Roll:

$$F_{low\ speed} = F_0 \qquad [3.23]$$

$$F_{high\ speed} = 1/2 \cdot F_0 \qquad [3.24]$$

The indicative modified curves for heave and roll are as follows,

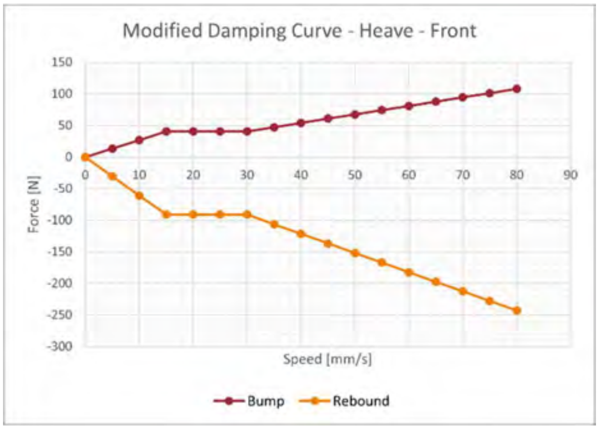

Figure 3.8: Modified damping curve for bump and rebound

Figures 3.9 – 3.12 represent the ideal modified damping curves for a range of damping ratios from 0.5 to 1. Shock absorbers have been tested for the majority of their settings, including both high and low speeds in compression and rebound. The results are compared with the ideal plots in order to match the desired behavior with the damper settings. These settings are used as the starting point for the vehicle tests on track during the suspension set up process.

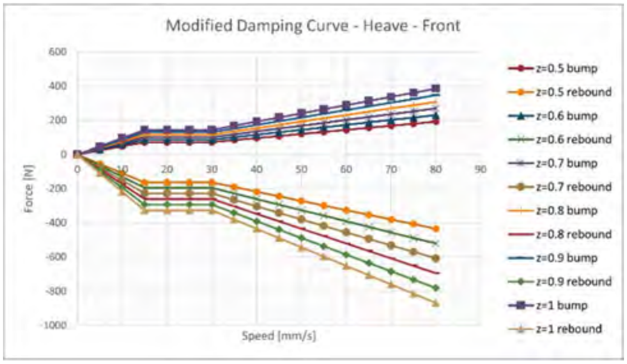

Figure 3.9: Damping curve of the front heave damper

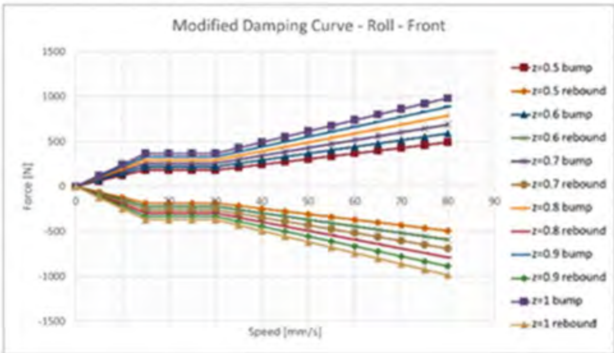

Figure 3.10: Damping curve of the front roll damper

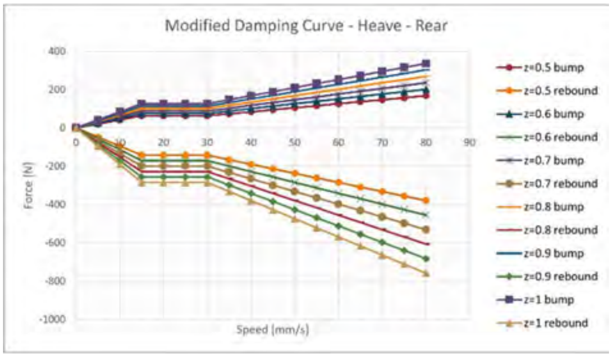

Figure 3.11: Damping curve of the rear heave damper

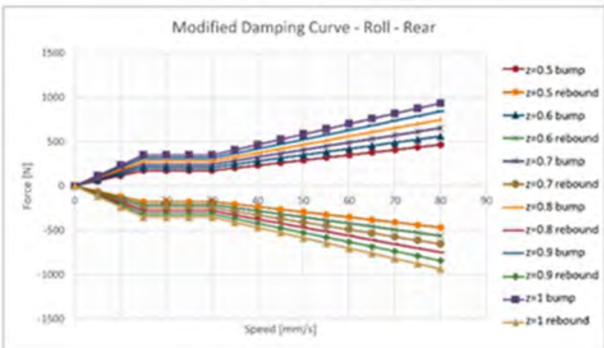

Figure 3.12: Damping curve of the rear roll damper

3.3 Suspension systems

3.3.1 Conventional suspension system

Conventional suspension system consists of one pair of spring and damper on each wheel and the anti-roll bar. Both springs contribute to all modes of the vehicle and the anti-roll bar acts as an additional spring in roll. The springs of each axle interact in parallel in heave and roll, whereas R-bar interacts in series with them.

3.3.2 Decoupled suspension system

The suspension system of the current study is a double unequal wishbone decoupled system. The decoupled mechanism separates the main two motions of the chassis. Heave or pitch and roll are controlled from a unique set of spring and damper. Similar studies [33] serve as validation to the analysis of the decoupled system that presented.

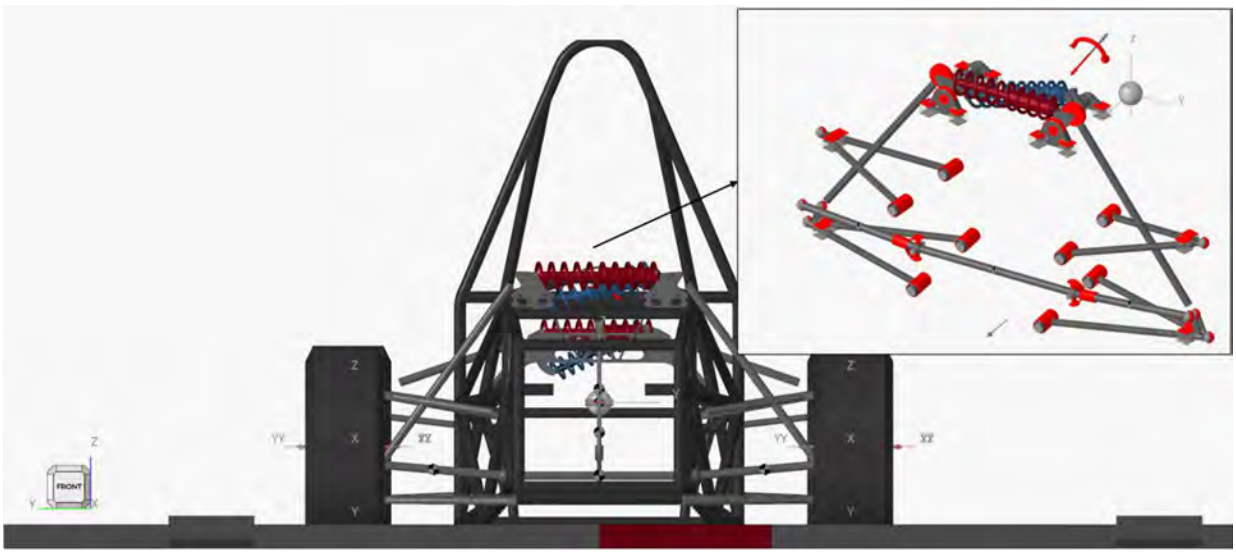

Figure 3.13: Elops suspension with the decoupled suspension system

3.3.2.1 Quarter car model of the decoupled suspension

Invoking the lateral symmetry of the suspension, the quarter of the car is isolated.

The vehicle is cut in the symmetrical plane along X axis. Each set of spring and damper interacts as two separate connected in series. One at each side.

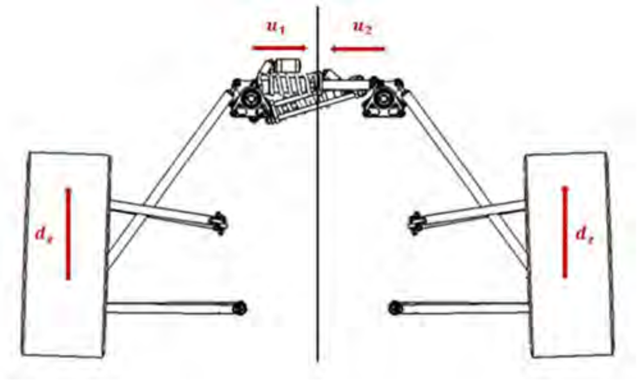

Figure 3.14: Wheel and spring displacement of the decoupled system

Conducting the analysis of two springs in series the following equations derived. The total spring displacement (u) is calculated by the sum of the two induced elements.

$$u = u_1 + u_2 \Rightarrow \frac{F}{k_{total}} = \frac{F_1}{k_1} + \frac{F_2}{k_2} \overset{F=F_1=F_2}{\Rightarrow} \frac{1}{k_{total}} = \frac{1}{k_1} + \frac{1}{k_2} \overset{k_{half}=k_1=k_2}{\Rightarrow} k_{total} = \frac{k_{half}}{2} \qquad [3.25]$$

Where k_{total} is the actual stiffness of the spring and k_{half} is stiffness of the quarter model.

Combining with equation [3.3] occurs:

$$k_{total} = \frac{WR \cdot MR^2}{2} \qquad [3.26]$$

The equation [3.18] is used for both heave/pitch and roll modes, substituting the corresponding motion ratios.

Similarly, the same process is followed for the damper.

$$c_{total} = \frac{c_{half}}{2} \qquad [3.27]$$

Where c_{total} is the actual damping coefficient and c_{half} is the damping coefficient of the quarter model.

3.3.2.2 Spring selection

The pre-simulation process begins with setting the range of spring rates that will be used, in front and rear. Taking the equation [3.5], $m_{s-front}$ and m_{s-rear} are defined.

Since the study concerns the quarter of the model, the sprung masses represent their half value (left or right).

In order to extract the heave spring stiffness, a frequency range is set between 2.5 to 5.5 Hz. For the calculations, the equations [3.3] to [3.5] are repeated backwards.

$$[3.5] \Rightarrow K_R = \left(f_s \cdot 2 \cdot \pi\right)^2 \cdot m_s \quad [3.28]$$

$$[3.4] \Rightarrow WR_{heave} = \frac{K_R \cdot K_T}{K_R - K_T} \quad [3.29]$$

$$[3.3] \Rightarrow SR_{heave} = \frac{WR_{heave} \cdot MR^2}{2} \quad [3.30]$$

Roll Rate is calculated via Roll Gradient (RG) which is the roll angle per lateral acceleration and Moment (M) due to lateral force.

$$RG = \frac{\theta}{a_y} \quad [3.31]$$

Where θ is Roll Angle and a_y is lateral acceleration.

$$M = m_s \cdot a_y \cdot \left(CG_{zSM} - RC_z\right) \quad [3.32]$$

Where CG_{zSM} is z coordinate of the suspended mass CoG and RC_z is z coordinate of the Roll Center.

Aiming to achieve lateral acceleration approximately 1.7g and restricting the roll angle to maximum 1 deg, a roll gradient spectrum close to 0.6 deg/g is set.

Total roll rate $K_{\Phi-total}$ [Nm/deg] is the sum of roll rate front and rear.

$$K_{\Phi-total} = K_{\Phi-front} + K_{\Phi-rear} \quad [3.33]$$

As a result of lateral moment and roll angle, the total roll rate can be determined.

$$K_{\Phi-total} = \frac{M}{\theta} \quad [3.34]$$

Finally, the spring stiffness front and rear is specified by the lateral load transfer distribution, λ.

$$K_{\Phi-front} = K_{\Phi-total} \cdot \lambda \quad [3.35]$$

$$K_{\Phi-rear} = K_{\Phi-total} \cdot \left(1 - \lambda\right) \quad [3.36]$$

Wheel rate for roll arises from anti roll moment according to the following equation.

$$K_{\Phi} = \frac{WR_{roll} \cdot K_T}{WR_{roll} + K_T} \cdot \delta \cdot \frac{track}{2} \cdot 2 \qquad [3.37]$$

Where wheel displacement (δ) is defined through roll angle.

$$\delta = \tan\theta \cdot \frac{track}{2} \qquad [3.38]$$

Recalling the equations [3.28], [3.29], [3.30] roll spring stiffness (SR_{roll}) is defined for both front and rear axle.

$$SR_{roll-front} = WR_{roll-front} \cdot MR_{front}{}^{2} \qquad [3.39]$$

And

$$SR_{roll-rear} = WR_{roll-rear} \cdot MR_{rear}{}^{2} \qquad [3.40]$$

3.4 Tire modelling

3.4.1 Mathematical model of tires: Pacejka '96

Tire stiffness and damping are crucial factors in understanding the dynamic behavior of a vehicle and how it interacts with the road surface. These properties play a significant role in determining a vehicle's handling characteristics, ride comfort, and overall-behavior. Tire stiffness and damping are sensitive to the variation of significant factors, including camber, slip angle, slip ratio, pressure, vertical load and excitation frequency. The Magic Formula is not a predictive tire model but is used to empirically represent and interpolate previously measured tire force and moment curves. It has quickly become a very popular tire model to describe the steady-state forces and moment occurring under various slip conditions.

Tires are designed to perform optimally at a specific range of temperature and tread depths. A tire outside its material's temperature spectrum loses flexibility and potential grip, while a properly warmed tire can provide better damping, absorbing the excitation from road irregularities. These characteristics are rather difficult to approach and in most simulations are totally neglected.

The forces and moments at contact patch can be calculated in MATLAB, or any coding environment. The most common tire model is the Pacejka '96, or Magic Formula [11, 23 - 26, 32]. According to this model, the same mathematical equation can be used to predict lateral and longitudinal ground forces as well as self-aligning torque and overturning moment, for both single and combined slip conditions.

The Magic Formula provides accurate results for lower frequency road profiles, which for instance are lateral and longitudinal slopes, like banks and grades. These profiles introduce vibrations of frequencies less than 8 Hz. Roads which consist of discrete irregularities, such as curbs, joints, potholes or cracking zones, result in frequencies up to 80 Hz. Under these conditions the tires are deformed due to their elastic properties and a Rigid Ring Model shall be used to describe them.

The inputs for these calculations are slip angle, slip ratio, inclination angle with respect to the road surface, normal load and pressure. The formula used to describe the tire behavior is quoted below.

$$F_y = D_y \cdot \sin\left[C_y \cdot \tan^{-1}\left\{B_y a_y - E_y \cdot \left(B_y a_y - \tan^{-1}\left(B_y a_y\right)\right)\right\}\right] + S_{Vy} \qquad [3.41]$$

- D_y: Related with the coefficient of friction
  $D_y = F_z \cdot \left(p_{DY1} + p_{DY2} df_z\right) \cdot \left(1 - p_{DY3} Y_y^2\right) \cdot \lambda_{\mu y}$
  where, F_z: The vertical load in N and
  p_{DYi}: Pacejka model coefficients exported from tire test experiments.

- d_{fz}: Normalized variation in vertical load
  $d_{f_z} = \frac{F_Z - F_{Z0}}{F_{Z0}}$
  where, F_{Z0}: Nominal wheel load in N

- γ_y: Wheel inclination angle (radians)

- $\lambda_{\mu y}$: User scaling factor on coefficient of friction

- C_y: Shape factor
  E_y: Curvature factor
  These two define the shape of the curve at peak region

- B_y: Stiffness factor

- S_{Hy}: The horizontal offset of the curve at the origin

- S_{Vy}: Vertical offset of the curve at the origin

More details of this analysis would diverge from the purpose of this study. However, it is worth mentioning that the coefficients required to calculate the forces are accrued from experiments [25]. The SAE tire axis system is used through this study.

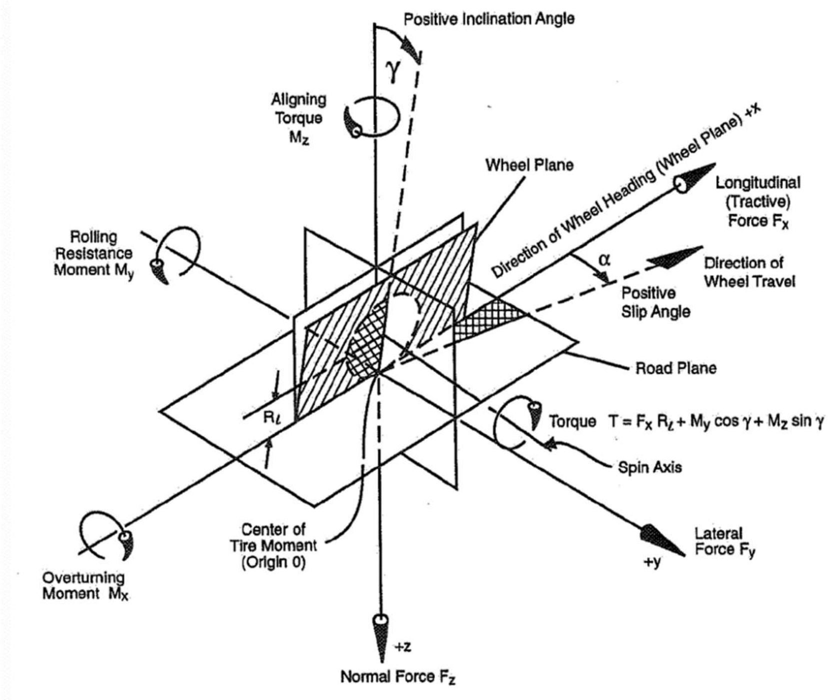

Figure 3.15: Tire coordinate system

The normal pressure distribution has an elliptical shape along the contact patch surface. Linear deformation can be formulated using elastic deformation equations as they are described by Hooke's law. The linear range of the contact patch forces lasts only until a peak where the friction can no longer resist the tangential stresses. Further apart, for higher slip angles the rear part of the contact patch starts sliding along the ground and its behavior cannot be described by the elastic equations.

3.4.2 Tire analysis

The study on the tires includes the analysis of their induced forces when the wheels are subjected to different conditions [26 – 27]. For this reason, the following parameters are implemented.

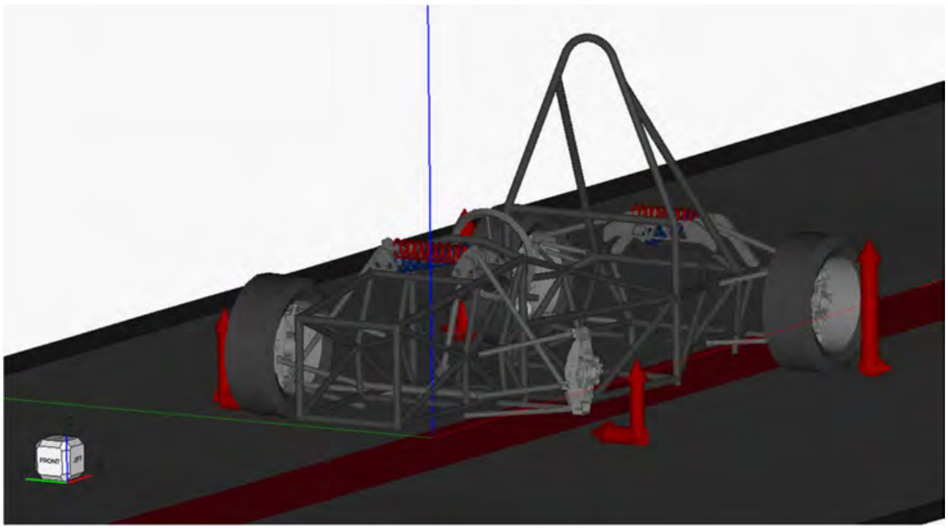

Figure 3.16: Tire external loads from a rough road profile

3.4.2.1 Slip ratio

The difference in rotational speed between a driving wheel and a free rolling wheel is described by the slip ratio and causes a deformation at the contact patch area.

$$slip\ ratio = \frac{\Omega \cdot R - V_{wheel}}{V_{wheel}} \tag{3.42}$$

The variation of this longitudinal tire force over slip ratio percentage is described by the following diagram.

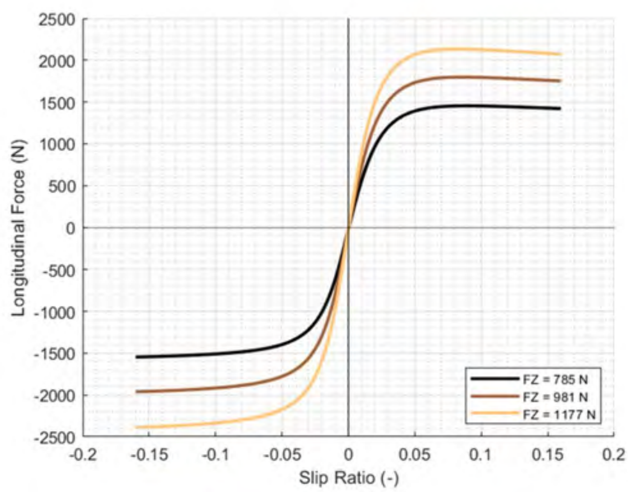

Figure 3.17: Longitudinal force vs slip ratio over normal loads

Longitudinal tire force divided by normal load expresses the longitudinal coefficient of friction. Positive value represents the effect of traction control while negative corresponds to the operation range of anti-lock braking system. For better understanding the following diagram is implemented.

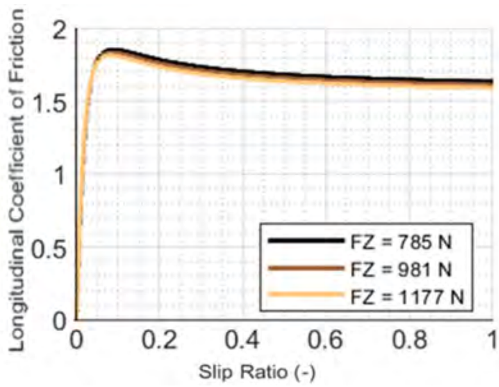

Figure 3.18: Longitudinal coefficient of friction vs slip ratio

3.4.2.2 Slip angle

Slip angle is defined as the difference between the car's heading and the tire's velocity vector or steering angle.

$$slip\ angle = \delta_{wheel} - \tan^{-1}\frac{V_y}{V_x} \qquad [3.43]$$

3.4.2.3 Tire forces and moments

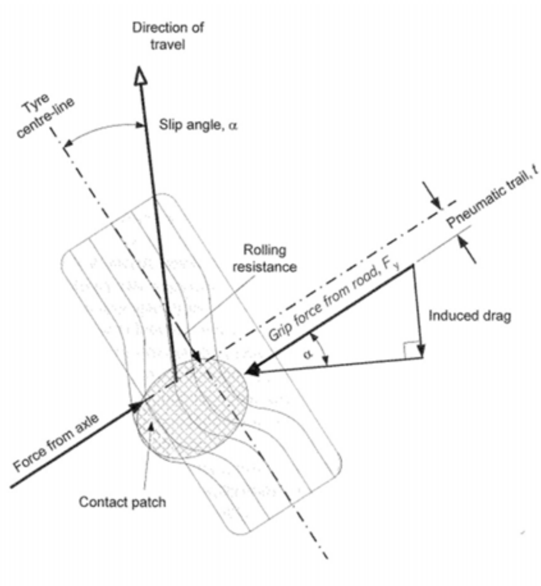

Figure 3.19: Contact patch deformation

Due to contact patch deformation, the F_y acts at an offset distance 't: pneumatic trail' from centerline. Its variation as the slip angle increases is highlighted below for three different normal loads.

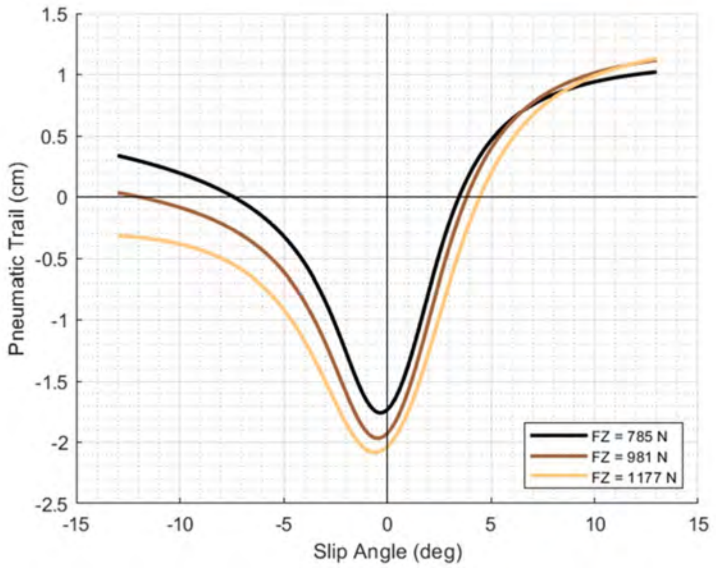

Figure 3.20: Pneumatic trail vs slip angle

Pneumatic trail leads to a moment generated around steering or vertical axis, called self-aligning torque (M_z). The amount of aligning torque is significantly reduced in the non linear ranges of slip angles.

$$M_z = F_y \cdot t \quad [3.44]$$

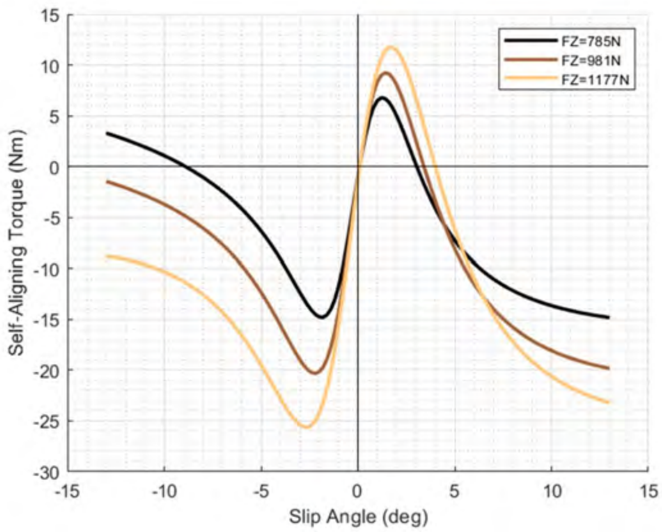

Figure 3.21: Self - aligning torque vs slip angle

Lateral force F_y can be described by two coordinates. The first is parallel to the direction of travel and called induced drag. This is applied in the opposite direction to the speed and results in deceleration when slip angle exists. The second is perpendicular to the direction of travel is the centripetal force. Rolling resistance and induced drag cause the total drag on tire. Lateral force over slip angle variation for different normal loads is represented in the plot below.

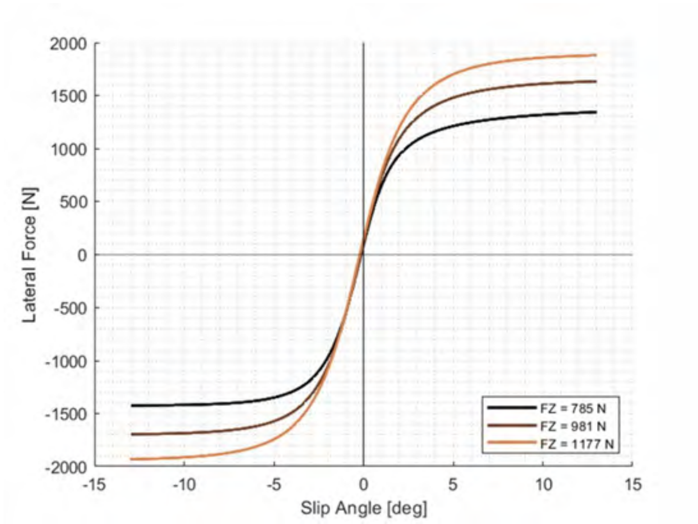

Figure 3.22: Lateral force vs slip angle

The lateral force divided by the normal load results in the lateral coefficient of friction. Its behavior over slip angle appears in the following diagram. It is observed that the peak lateral force coefficient of friction is higher for lower normal loads and lower for the heavier loads. This reduction is observed due to tire load sensitivity.

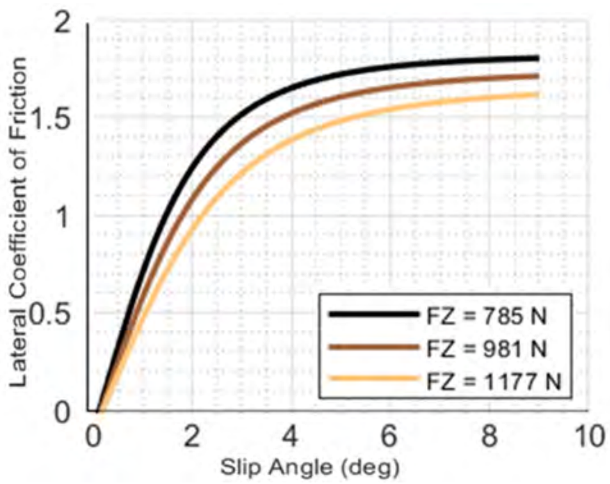

Figure 3.23: Lateral coefficient of friction vs slip angle over normal loads

3.5 Moments on vehicle's body

The present chapter, describe the moments around the three axis of the vehicle while external load act on the contact patch of the tire [23 - 24, 28-32].

3.5.1 Yaw moment – Torque around vertical axis

So far, it was comprehended that the road irregularities cause forces on each tire with coordinates on x, y and z axis. These forces result in the generation of moments around the tire's coordinate system since the tire's contact patch is deformable. The external excitation can make the car deviate from its path by an angle named body slip angle, β. The body slip angle defines the direction of the travel. The driver needs to adjust the steering so as the vehicle to stay on course. This input induced by the driver is the steering angle, δ_{wheel}.

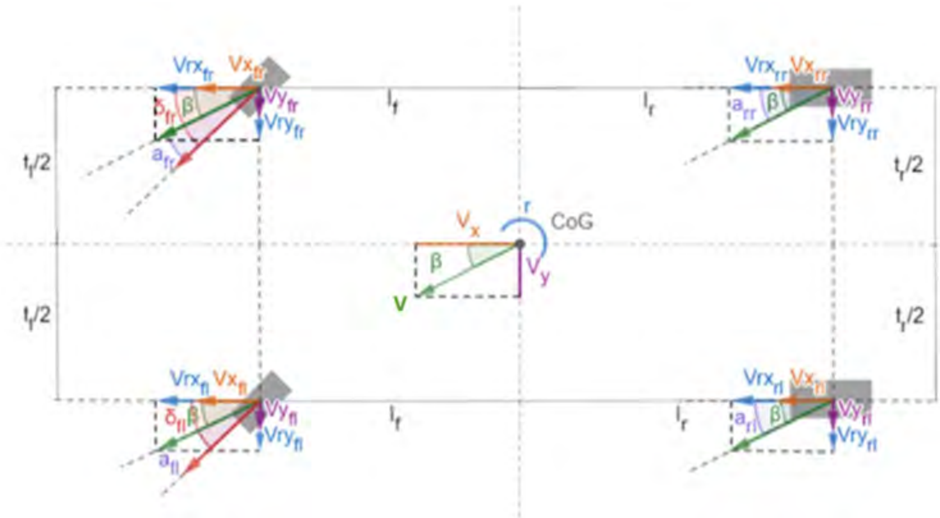

Figure 3.24: Velocity vectors on tires as function of body slip angle

As it is described in the chapter [3.4.2.2], the difference between the steering angle and the body slip angle, is the slip angle a. For a vehicle speed V and yaw rate equal to r, the slip angles a_{ij} of each tire can be calculated.

$$a_{fl} = \delta_{fl} - \beta = \delta_{fl} - \tan\left(\frac{V_y + r \cdot l_f}{V_x + r \cdot \frac{t_f}{2}}\right) \qquad [3.45]$$

$$a_{fr} = \delta_{fr} - \beta = \delta_{fr} - \tan\left(\frac{V_y + r \cdot l_f}{V_x + r \cdot \frac{t_f}{2}}\right) \qquad [3.46]$$

$$a_{rl} = \delta_{rl} - \beta = \delta_{rl} - \tan\left(\frac{V_y + r \cdot l_r}{V_x + r \cdot \frac{t_r}{2}}\right) \quad [3.47]$$

$$a_{rr} = \delta_{rr} - \beta = \delta_{rr} - \tan\left(\frac{V_y + r \cdot l_r}{V_x + r \cdot \frac{t_r}{2}}\right) \quad [3.48]$$

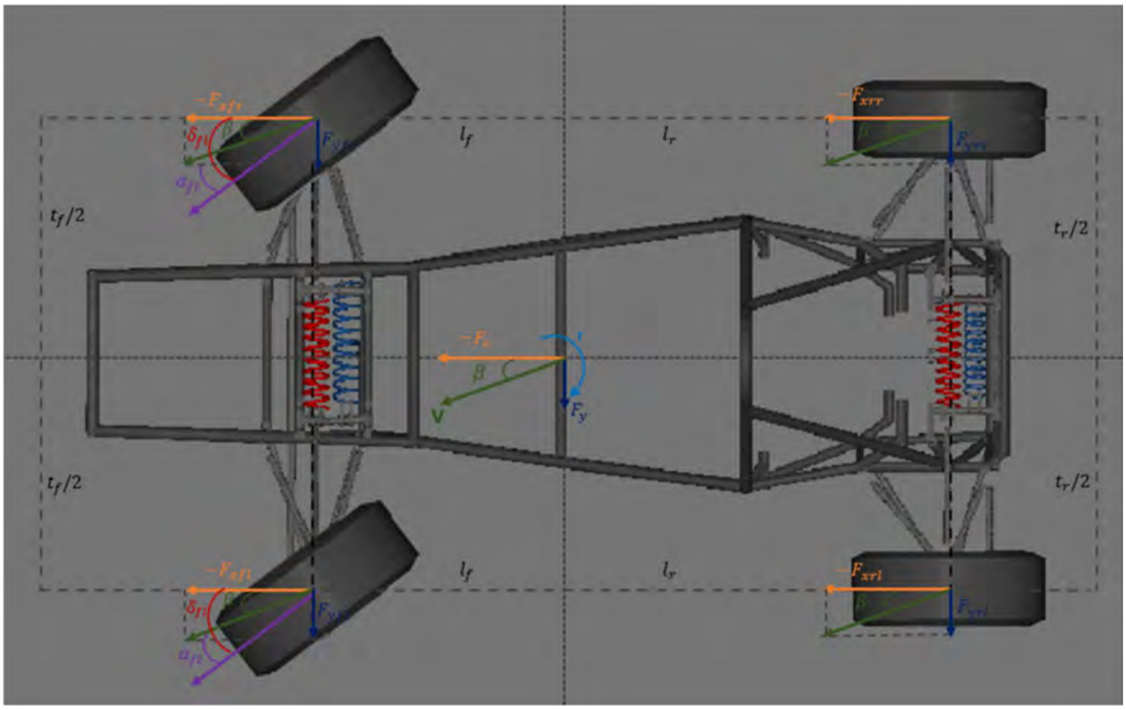

Figure 3.25: Force vectors on tires as function of body slip angle

The lateral and longitudinal force transferred in the car's CoG is the combination of the forces from the four tires.

$$F_y = \cos\delta \cdot \left(F_{y_{fl}} + F_{y_{fr}}\right) + \sin\delta \cdot \left(F_{x_{fl}} + F_{x_{fr}}\right) + F_{y_{rl}} + F_{y_{rr}} \quad [3.49]$$

$$F_x = \sin\delta \cdot \left(F_{y_{fl}} + F_{y_{fr}}\right) + \cos\delta \cdot \left(F_{x_{fl}} + F_{x_{fr}}\right) + F_{x_{rl}} + F_{x_{rr}} \quad [3.50]$$

Yaw Moment (*N*) is actually the resultant moment around the vertical axis that passes through the center of gravity of the car. It is the outcome of lateral and longitudinal forces and self-aligning torque acting on the contact patch when the vehicle tends to deviate from its patch or to follow a curved path. This moment is formulated as,

$$
\begin{aligned}
N &= \left(\left(Fy_{fl} + Fy_{fr}\right)\cdot \cos\delta - \left(Fx_{fl} + Fx_{fr}\right)\cdot \sin\delta\right)\cdot l_f \\
&= -\left(Fy_{rl} + Fy_{rr}\right)\cdot l_r + \left(\left(Fy_{fl} - Fy_{fr}\right)\cdot \sin\delta + \left(Fx_{fl} - Fx_{fr}\right)\cdot \cos\delta\right)\cdot \frac{t_f}{2} \\
&= +\left(Fx_{rl} - Fx_{rr}\right)\cdot \frac{t_r}{2} - Mz_{fl} - Mz_{fr} - Mz_{rl} - Mz_{rr}
\end{aligned}
\qquad [3.51]
$$

3.5.2 Roll moment – Torque around longitudinal axis

3.5.2.1 Lateral load transfer

In road course events, the forces on the tires result in a variation of the loads on the vehicle. Apparently, the weight of the car doesn't change, but its distribution is affected by the external loads, caused by either the roughness of the road or the path it follows. The road irregularities which are the main topic of this paper, can generate a wide range of load cases. Their shape along the length of the road can affect the direction of the resultant forces acted on each tire and therefore the total forces and moments on the car. The load transfer can be measured in all axes, knowing the acceleration of the vehicle at the center of mass and its geometrical characteristics. The distribution of this load between front and rear axle is affected by the suspension geometry and track width. In front view the steady state load transfer can be formulated below.

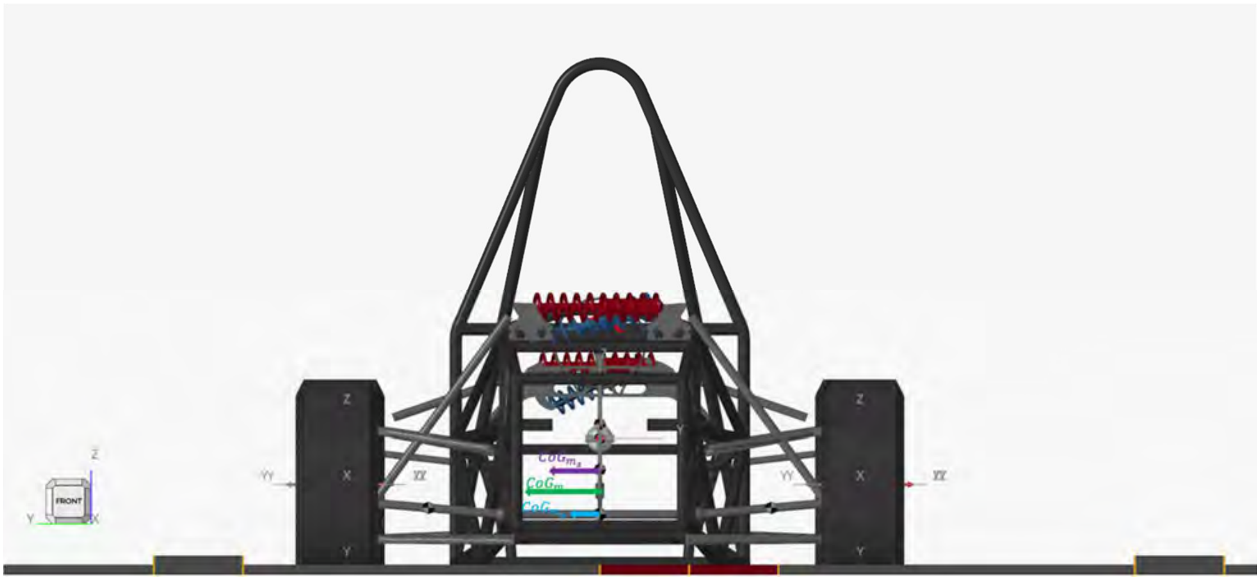

Figure 3.26: Load transfer distribution between suspended and non suspended mass

$$Lateral\ Load\ Transfer = \frac{m \cdot a_y \cdot CoG_z}{track} \qquad [3.52]$$

- m, is the total mass of the car.
- a_y, is lateral acceleration.
- CoG_z, is the height of the center of mass.
- $track$, is the width of the car between wheels contact patches.

The load transfer consists of two entities, the suspended and non-suspended load transfer.

$$LLT_{m_s} = \frac{m_s \cdot a_y \cdot CoG_{zSM}}{track} \qquad [3.53]$$

$$LLT_{m_u} = \frac{m_u \cdot a_y \cdot CoG_{zNSM}}{track} \qquad [3.54]$$

$$Lateral\ Load\ Transfer = LLT_{m_s} + LLT_{m_u} \qquad [3.55]$$

The measure of contribution of suspension geometry to the load transfer is explained by separating the suspended load transfer to the geometric and the elastic one. This simplification is effective if the lateral force applied at the suspended mass CoG is replaced by a force acting on the roll center and a moment applied at roll center as well. The lateral load transferred through suspension links causes the geometric load transfer and the roll moment is responsible for the elastic one.

$$LLT_{m_s} geometric = \frac{m_s \cdot a_y \cdot RC_z}{track} \qquad [3.56]$$

$$LLT_{m_s} elastic = \frac{m_s \cdot a_y \cdot (CoG_{zSM} - RC_z)}{track} \qquad [3.57]$$

Where RC_z, is the height of the roll center of the car. The z coordinate is not always the same front and rear, which means the car does not rotate along x direction. If the elastic load transfer is zero, the total lateral load is transferred through the links and no roll angle or roll moment is affected.

3.5.2.2 Roll moment calculation

Front and rear roll centers along with the center of gravity position affect the lateral load transfer, how it is distributed on both axles and hence the amount of the chassis roll. As it is described in previous chapters, the resultant roll moment of the chassis can be modified by adjusting the springs stiffness or the suspension geometry characteristics.

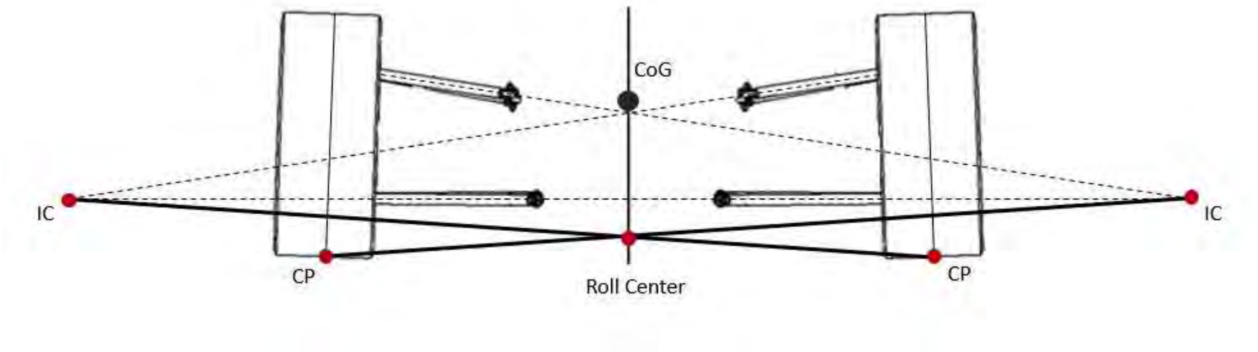

Figure 3.27: Geometrical definition of roll center

The distance (d) between the height of the center of gravity (CoG) and the roll center (RC) causes a moment around the latter one. The lateral force acted on the center of gravity due to the excitation force from the road irregularities generates a moment around the roll center and so makes the chassis roll. Similar to the behavior of the car when it is driven through a corner. To measure the position of the roll center, the front view of the car is isolated along with the suspension arms. The trajectory lines that follow the links direction of each side are crossed at the point known as instantaneous center. Now, the lines connect the instant center to the tire's contact patch at each side are crossed at the roll center position.

For a specific amount of lateral acceleration (a_y), the roll moment (M) is formulated as:

$$M = m_S \cdot a_y \cdot \left(CG_{zSM} - RC_z\right) \qquad [3.58]$$

To control the amount of chassis roll, the required amount of moment should be achieved by adjusting the spring stiffness settings and targeting in the most efficient suspension geometry.

3.5.3 Pitch moment – Torque around lateral axis

3.5.3.1 Longitudinal load transfer

Similar with the lateral movement, the longitudinal component of load transfer is calculated as,

$$LongLT_m = \frac{m \cdot a_x \cdot CoG_z}{l} \qquad [3.59]$$

- a_x, is longitudinal acceleration.

– l, is the length of the car between the front and rear wheel centers.

3.5.3.2 Pitch moment calculation

As the load is transferred between front and rear axle, longitudinal acceleration is produced. The body of the car rotates around the lateral axis and pitch movement occurs. It is the same behavior when a car is braking or accelerating.

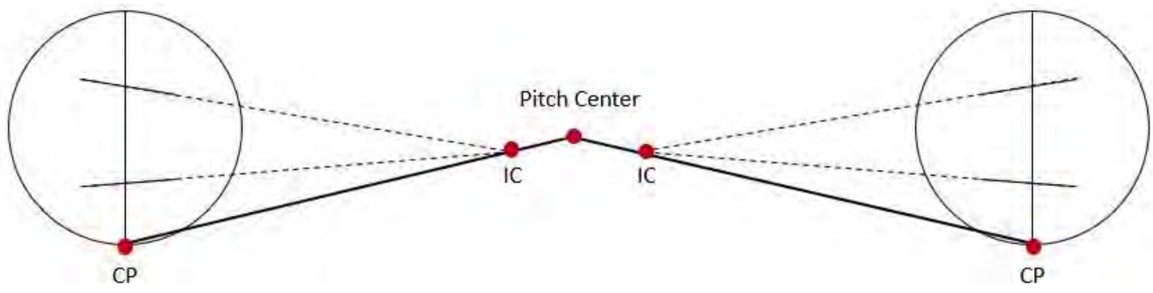

Figure 3.28: Geometrical definition of pitch center

In order to understand where the pitch centers of each axle are located the car is positioned in its side view, as it is represented in the picture above. The intersection point of the trajectory lines of the inner point of the suspension links at each axle is the instantaneous center. The pitch center is the cross point between the lines that connect the instant center and the tire's contact patch of each axle.

Anti-geometries are the percentage of load that is distributed between the suspension links and the heave springs. The geometry of the links creates a reaction force that absorbs part of the external load to transfer to the springs, preventing the vehicle from heave or pitch.

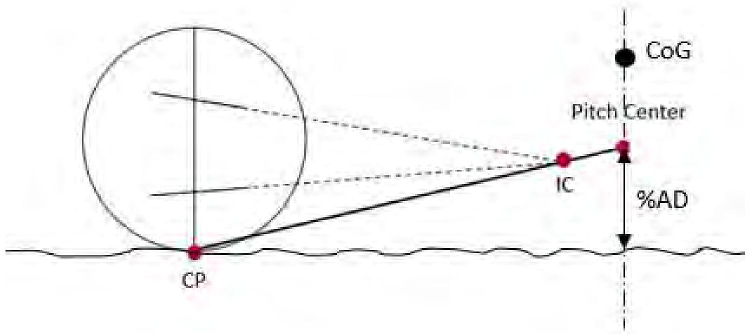

Figure 3.29: Anti - dive percentage

Anti-dive refers to the front suspension while anti-squat to the rear. The calculation is done based on the scheme above and these values are not necessarily equal. Anti-geometries have an important effect on the response of the system since they define the amount of load that passes through the springs.

3.6 Multibody model of an FSAE car and simulation results

The theoretical model of vehicles passing over roads with irregularities described in the previous paragraphs. A more analytical approach of this vehicle is developed and simulated using MotionView. The assembly of the car contains the primary structural components as they have been designed in a CAD software, as well as the mechanical parts that enclose the vehicle's movement. These components hold the actual materials and properties and they are simulated as flexible parts. The tire properties are imported through the related files (.tir files) which are recognized by the software. Additional subsystems which are required to simulate the events, such as the engine, differential and steering were imported from Altair's library. These additional components are rigid and only impart to the generation of motion. Therefore, stress and strain could not be measured at them, unless they will be imported as flexible parts. This solution would rapidly increase the computational time of the simulation and this effort would derive from the purposes of this study. The model is used for the simulation is a Formula Student Car with decoupled suspension system and double unequal wishbone arms. The basic suspension parameters of the vehicle that used in these simulations are shown in the below table.

Table 3.1: FSAE vehicle parameters

Component	Value
Tire dimensions	205/470 R13
Total mass (without driver)	208 kg
Unsprung mass	43.15 kg
Total mass distribution	45 % front
Suspended mass distribution	43 % front
Heave spring stiffness front	20 N/mm
Roll spring stiffness front	15 N/mm
Heave spring stiffness rear	35 N/mm
Roll spring stiffness rear	25 N/mm
Damping ratio	0.5
Tire stiffness	100 N/mm
Tire damping ratio	0.027

The connection between the subsystems and their components is enhanced by joints resulting in a model whose total movement is representative of reality. Any kind of connection or attachment with a fastener, such as the attachment of rocker supports to the chassis, or the inserts of wishbone arms to the carbon tubes, has been replaced by fixed joints. The relative motion of all suspension components, tires and chassis is determined through ball, revolute, or universal joints and bushings. Couplers have been implemented where relative motion between two joints is required. The use of the connectors at the front suspension system is indicated in the following picture.

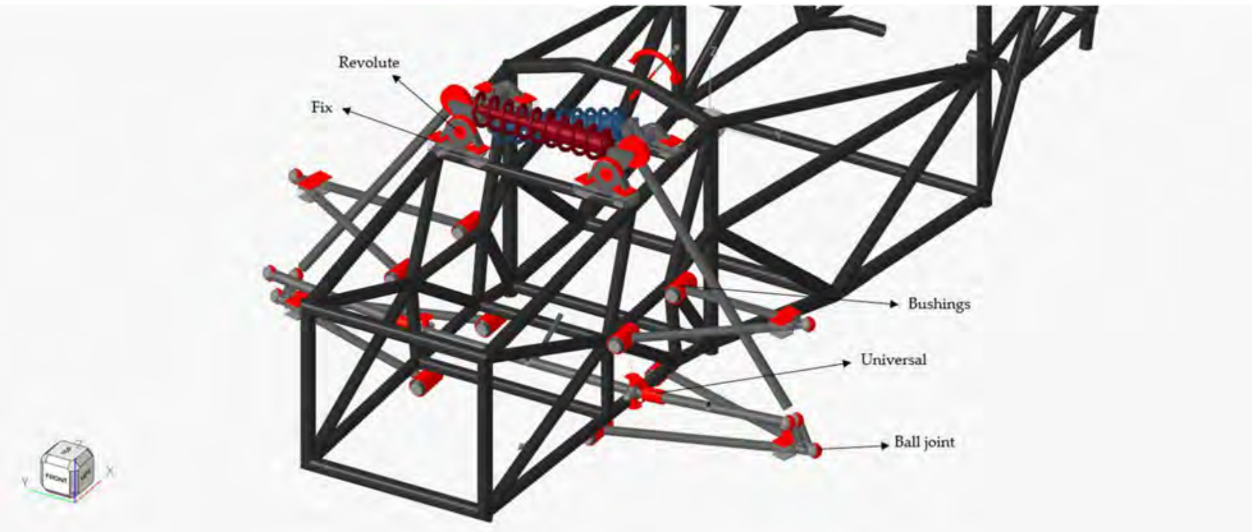

Figure 3.30: Connectors at the front suspension of the car

The multi body system is tested in straight roads at constant speed equal to 60 km/h. The specific road course event allows adjustability at the steering wheel whenever the external excitation tends to make the car deviate from its path. The road profiles are generated implemented the PSD method and the simulation process is conducted for three classes of irregularities, starting from the poorest quality (Class A) to the highest one (Class C). The spectrum of road roughness can cover a wide range of amplitudes and frequencies many of which are considered inappropriate for the dimensions of the simulated vehicle. The selected three cases are appeared in the below table and their profile along the length of the 256 meters road is plotted in the figure [3.31].

Table 3.2: Road irregularities classifications used for the MBD simulation

Road Class	$G_d(\Omega_0)\,(10^{-6}m^3)$	w
A	5.3	2.4
B	2.1	2.3
C	0.7	1.8

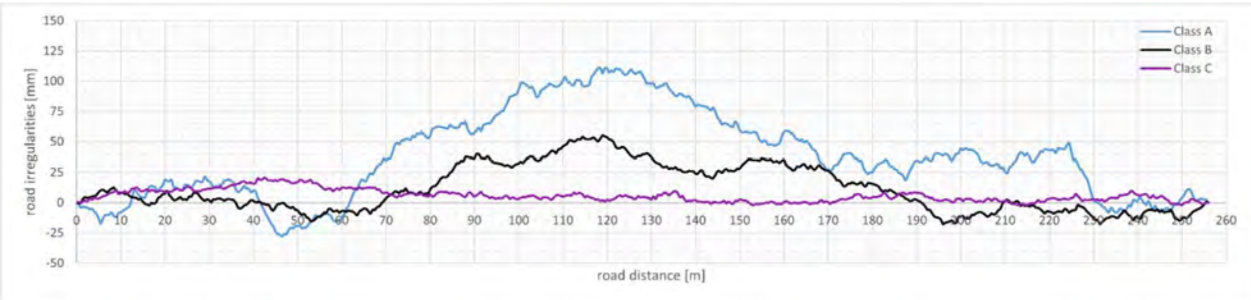

Figure 3.31: Road roughness profiles selected for the simulation

The simulation results provide a detailed review of the external loads and the response of the components that build the multibody system. The stress – strain contour is plotted on the surface of the components providing their dynamic values over time and position on the track. At the same time 2D graphs analyze the response of the overall system. The stress – strains are developed on the vehicle during the simulation are depicted below. The additional subsystems which mentioned earlier (engine, differential, etc.) are hidden for simplicity reasons. However, they contribute in total mass, mass distribution and inertia aiming to accomplish realistic results.

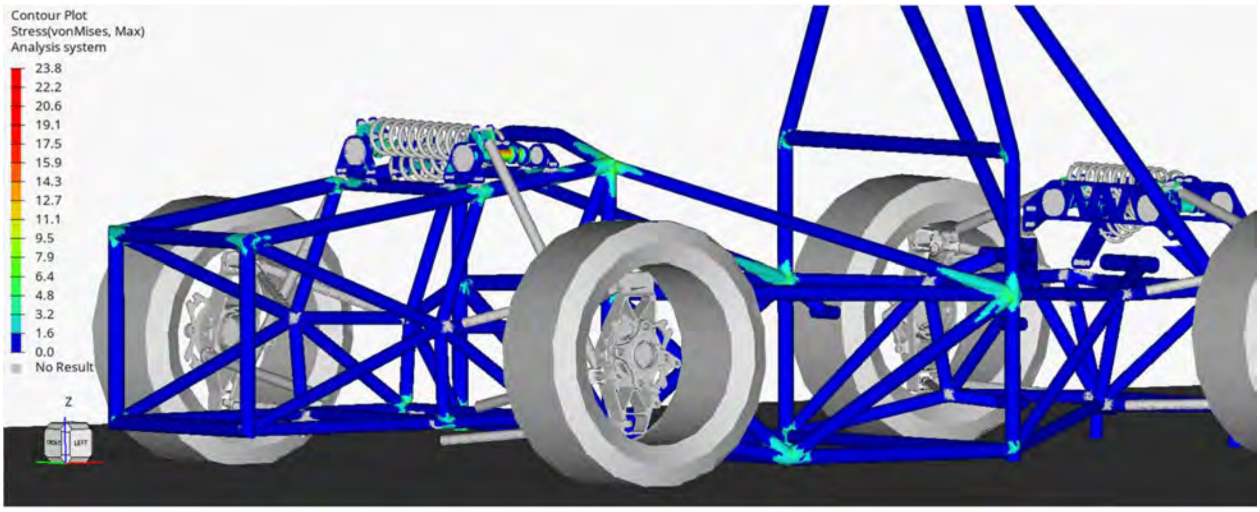

Figure 3.32: Stress contour [MPa] on selected components as the vehicle crosses the class A profile

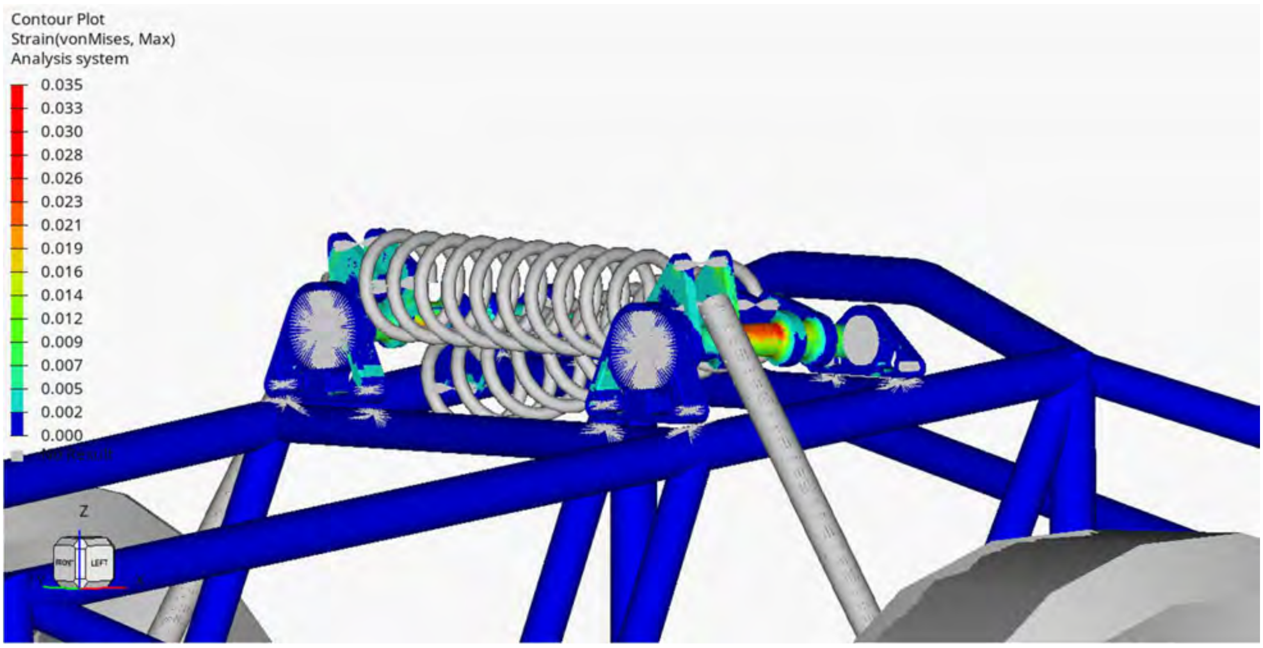

Figure 3.33: Strain contour on selected components as the vehicle crosses the class A profile

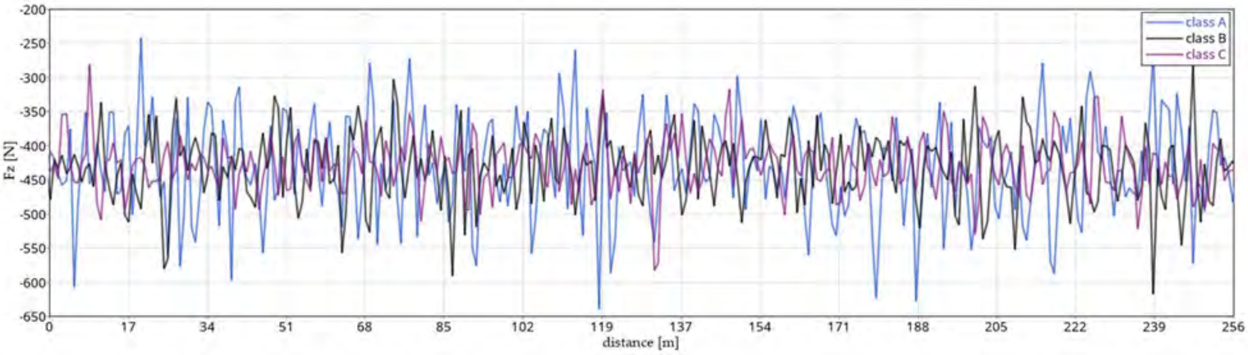

Figure 3.34: Normal load on front let tire contact patch vs position of the vehicle

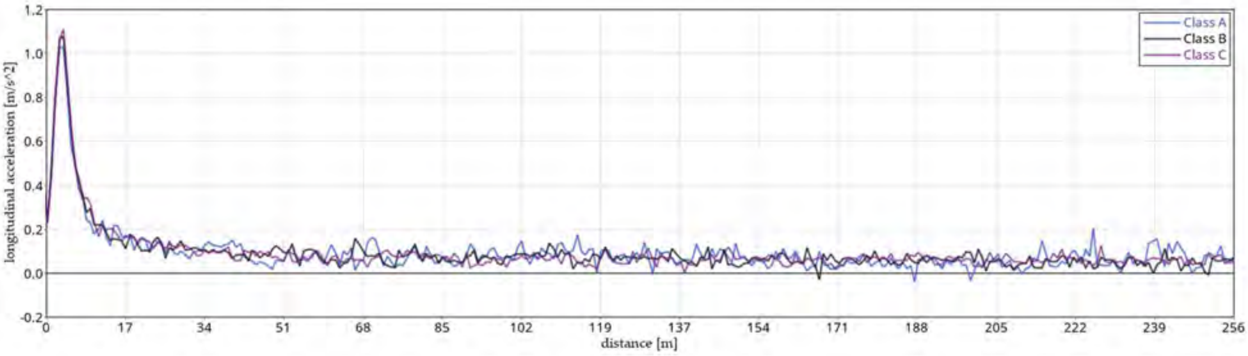

Figure 3.35: Longitudinal acceleration vs position of the vehicle

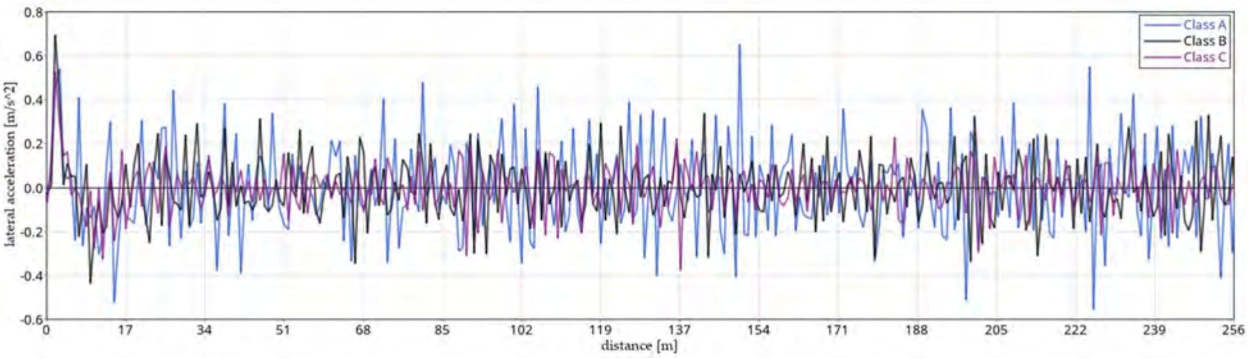

Figure 3.36: Lateral acceleration vs position of the vehicle

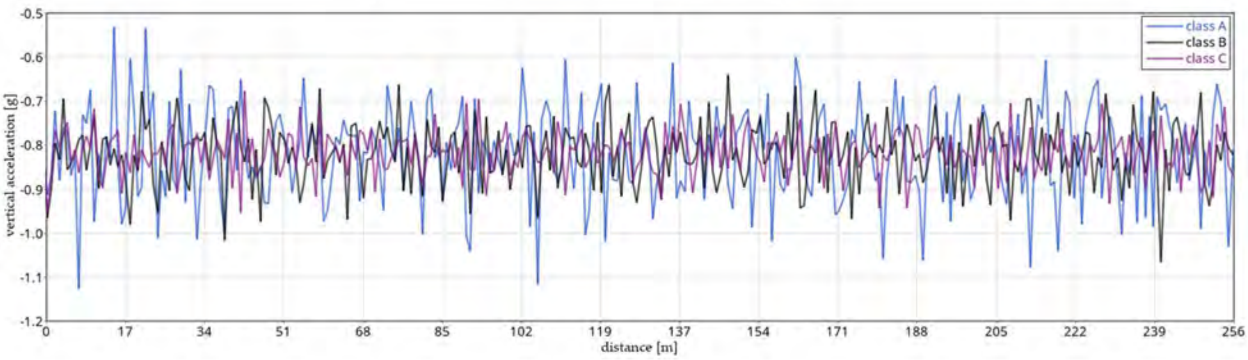

Figure 3.37: Vertical acceleration vs position of the vehicle

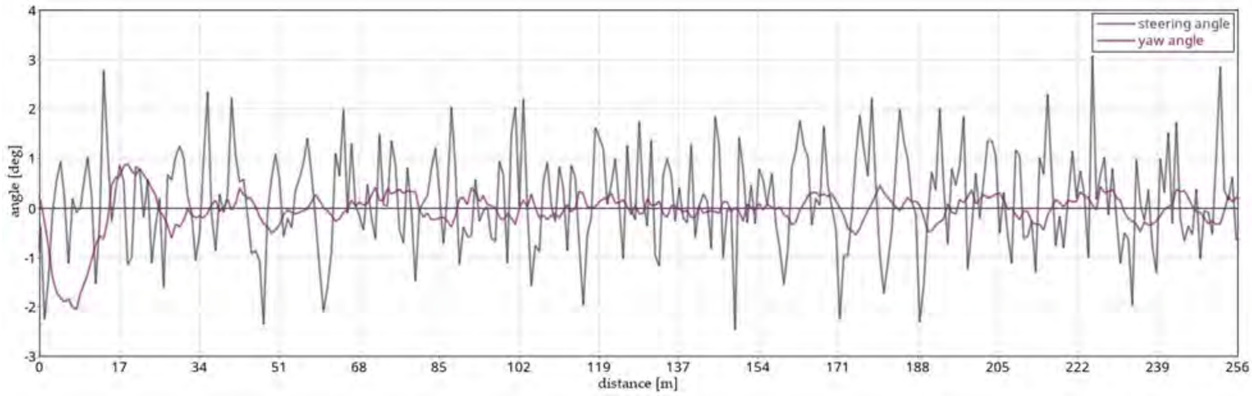

Figure 3.38: Yaw and steering angle vs position of the vehicle for Class A

From Figure 3.34 we extract a sample of the force that act on front left tire. The forces from the pavement create moment around z axis (yaw moment) and demand the driver's input to maintain the car on track, as explained in paragraph 3.5.1. Figure 3.38 show yaw angle oscillation together with the steering wheel adjustments.

Additionally, the contact patches are deformed. Figure 3.39 zooms in the distance range 110-150 m to compare the lateral deformation of all tires running in class A road.

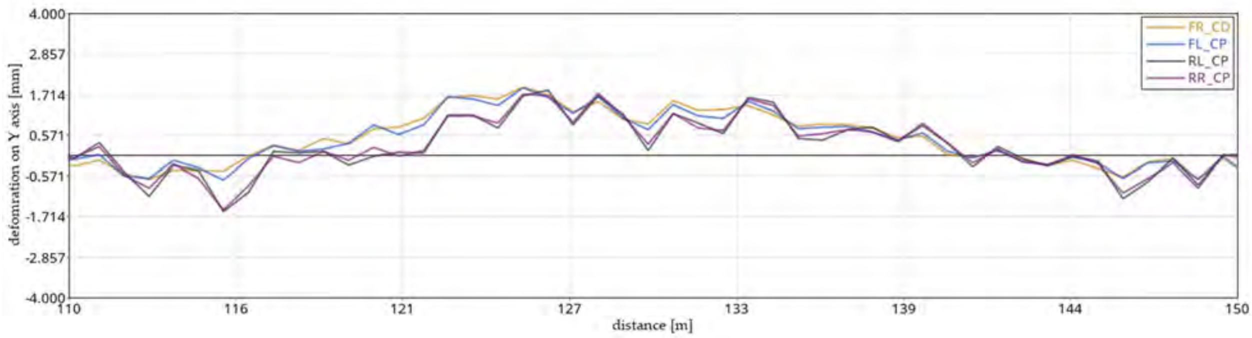

Figure 3.39: Contact patch lateral deformation for Class A

Multibody dynamic simulations demand an in depth analysis in the suspension of the car. The tires are the key factor as they provide the only contact of the car with the road. The forces that they receive are analyzed in three dimensions while their deformation is taken into account when calculating the resultant response of the car. The geometry of the suspension system, including parameters, such as motion ratio, define the kinematic boundaries of the car. Finally, springs and dampers complete the connection between sprung and unsprung masses. Their contribution is extremely critical, especially if the system is analyzed as deformable, helps in their proper selection.

The kinematics of the vehicle defines the joints between the components. The rod-ends, ball bearings, revolute bearings which are used in the real vehicle have been selected after conducting structural analysis and assuring alliance with the FSAE rules. For example, all threaded critical fasteners must be at grade 8.8 or stronger. In the current thesis, this analysis was purposely neglected and all joints are considered as rigid. Carbon wishbones and pushrods are also considered as rigids. This assumption has been confirmed after simulating the vehicle with and without these flexible components in class A profile and comparing the results. The identical behavior in the acceleration and displacement measurements in the COG (less than 3% deviation), leads to a safe conclusion.

The lower the quality of the road the harder the impact on the vehicle, which can be improved by changing the settings of springs and dampers or tires dimensions and properties. The optimization of these elements and their response wasn't a scope of this thesis.

In summary, this tool allows the detailed representation of a real vehicle, able to be simulated in different conditions. The engineers can simulate their car not only on straight road, but also on plenty of events and focus on the case they want to study. Results about the structural integrity of the components and the load cases acting on them can be extracted. At the same time the tool allows the optimization of car's parameters in terms of proper behavior under these conditions, safety and even performance.

Chapter 4

Summary

4.1 Conclusions

This study aims to create tools for analyzing the effects of road irregularities on vehicles. The impact of the loads that are produced can be analyzed not only for the structural integrity of the vehicle but also for the road. Especially when the road is an oscillated bridge, the mass of the vehicle, its average speed and the external excitation force due to roughness has to be taken into consideration. This study has been channeled into two cases, the vehicle bridge interaction and the generation of a 3D multi-body vehicle.

The VBI model was set in MATLAB. Using as a bridge an Euler-Bernoulli simply supported beam which was developed using finite element methods. The irregularities of the road surface were also considered since their excitation is the main contributor for the generated load case. In the graphs, the results on the midpoint of the bridge are studied. The effects of the roughness and the vehicle's speed can be compared, neglecting or not the contribution of gravity forces. Also, its response is compared the bridge's stiffness (EI). Two schemes were used for modeling the vehicle, a simplified 2-DOFs with one contact wheel and a 4-DOFs with two wheels. The plots contain information for the response of both vehicles as they interact with the bridge, evaluating their influence on the midpoint's displacement and acceleration. The error between the two vehicles is lower than 16%, which is probably affected by the size of the vehicle compared to the size of the bridge. Moreover, a variation in the car speed seems that has a significant effect on the response of the bridge, especially when the car passes further than the half of the length of the bridge. The coupled system was solved using Newmark's -beta method and the results were presented in paragraph 2.8.

The multibody model was set using ALTAIR MotionView, while all the structural components were extracted from CAD software and contain their geometric and material properties. This study provides the theoretical background behind vehicle dynamics, including the analysis of the decoupled suspension system that is used in the model.

The car is simulated running on a straight path at a constant speed over three different road profiles. The roughness oscillates the vehicle, causing yaw angle variation and forcing the driver to perform steering adjustments, while the tire's deformation as seen in Figure 3.39 justifies the need for such a detailed analysis.

During post processing, the stress and strains are plotted on the components of the vehicle over time and distance. The areas of stress concentration are seen on the chassis in the connection of the tubes, as it runs in class A profile. The loads in these areas, are approximately 9 MPa, causing no significant deformation to the chassis. Front suspension rockers receive 23 MPa and the strains are measured at 0.03. Vehicle's structural stiffness allows to withstand such loads, but it is seen during simulations that reducing the quality of the road or increasing the vehicle's speed can cause failure. For example, when $G_d(\Omega_0)$ was set at 9.5 10^{-6} m^3 and w at 2.9 at 60 kph the front upright excited its yield strength.

4.2 Future work

The proposed future work concerns the advance of both the bridge and the vehicle model, while increasing their accuracy and usefulness in the industry.

The bridge subsystem in this thesis is 2D, while the nodes on the grid allow only rotational and translational motion. One step forward is the addition of the axial displacement of the beam maintain the current dimensions. The 3D representation of this case dictates a 7-DOFs vehicle (assuming there is no yaw angle and steering) and an oscillated plate as a bridge. The complexity of the latter is depended on its design. Three dimensional spaceframes or arc bridges constitutes a challenge for the engineer who studies this case. Of course, the use of a specialized software minimizes the effort of establishing comparable cases. Multibody simulations provide solutions for the above cases, combing the two subsystems.

Multibody simulations can be further developed across many directions. In the current study many the user can pay attention in the simplifications that have been done. Adding more structural components into the system or analyzing the joints effects when they are considered as non-rigid. Also, the powertrain system can be developed including the vibrations from the engine to the chassis.

Future target is also the analysis of road irregularities given the specific vehicle. As the vehicle is simulated on different profiles a data set of system's response can the gathered. This data can be used for training a neural network able to identify road qualities when the monitored vehicle passes over. The simulation results can also used for detecting the critical points to add sensors in the spaceframe chassis and in the rest of the components.

In the automotive, structural analysis of the components under dynamic loadcase can be done. In the effort to increase comfort and vibration isolation on passengers' cabin studies can be conducted taking into account active suspension systems. Automatic control theory can be applied to the car model, to serve the design of autonomous vehicles or for the generation of lap time simulation within the motorsport industry.

In general, the complexity of a multibody simulation can be significantly increased based on user's inputs. A useful methodology is the isolation of each subsystem when conducting analysis on specific components, such as structural analysis including all fasteners in the front suspension.

References

[1] Charikleia Stoura, "Analytical and numerical examination of the vehicle – bridge interaction problem in railway bridges", The Hong Kong University of Science and Technology, Department of Civil and Environmental Engineering, pp. 46, 59-63, 2021.

[2] Dimitrios Simos, "Dynamics of vehicle – bridge interaction system", University of Thessaly, Department of Mechanical Engineering, pp. 26-51, 62-66, 2022.

[3] Lu Sun, Xingzhuang Zhao, "Coupled dynamics of vehicle – bridge interaction system using high efficiency method", pp. 1-3, 7-13, 2021.

[4] Solmaz Pourzeynali, Xinqun Zhu, Ali Ghari Zadeh, Maria Rashidi and Bijan Samali, "Comprehensive Study of Moving Load Identification on Bridge Structures Using the Explicit Form of Newmark-β Method: Numerical and Experimental Studies", pp. 3-10, Sydney, 2021.

[5] Urszula Ferdek, Jan Łuczko, "Vibration analysis of a half – car model with semi – active damping", Cracow University of Technology, Faculty of Mechanical Engineering, Krakow, Poland, JOURNAL OF THEORETICAL AND APPLIED MECHANICS 54, 2, pp. 323-324, 326-327, 2016.

[6] Costas Papadimitriou, "Lectures of Vibrations and Dynamics of Machines", University of Thessaly, Department of Mechanical Engineering.

[7] Spyros A. Karamanos, "Lectures of the Finite Element Methods", University of Thessaly, Department of Mechanical Engineering.

[8] Manfred Mitschke, Henning Wallentowitz, "Dynamik der Kraftfahrzeuge", Springer, vol. 5, pp. 343, 2014.

[9] Fan Feng, Fanglin Huang, Weibin Wen, Zhe Liu, Xiang Liu, "Evaluating the dynamic response of the bridge – vehicle system considering random road roughness based on the moment method", China, 2021.

[10] Akshay Bhardwaj, Daniel Slavin, John Walsh, James Freudenberg, R. Brent Gillespie, "Rack force estimation for driving on uneven road surfaces", Mechanical Engineering & Electrical and Computer Engineering, University of Michigan, pp. 2-3, 2020.

[11] Justin Madsen, Alex Dirr, “Comparison of a steady-state Magic Formula tire model with a commercial software implementation”, Technical Report TR-2014-14, pp. 6-7, 2014.

[12] M. Agostinacchio, D. Ciampa, S. Olita, “The vibrations induced by surface irregularities in road pavements – a Matlab® approach”, Eur. Transp. Res. Rev. (2014), pp. 267-270, 2013.

[13] George Lindfield, John Penny, “Numerical methods using Matlab®”, pp. 265-268, 2019.

[14] Fengzong Gong, Fei Han, Yingjie Wang, Ye Xia, “Bridge damping extraction method from vehicle – bridge interaction system using double – beam model”, Appl. Sci. 2021, pp. 7.

[15] Junjie Xu, Yuli Huang, Zhe Qu, “The high frequency oscillation in systems with Rayleigh damping model”, 12th CCEE 2019, pp. 1-2.

[16] “Finite element notes, Lamped and consistent mass matrices”, University of South Australia, pp 31-9.

[17] Y. B. Yang, J. D. Yau, Y. S. Wu, “Vehicle – Bridge Interaction Dynamics With Applications to High - Speed Railways”, World Scientific Publishing Co. Pte. Ltd., pp. 175-196, 2004.

[18] Elias G. Dimitrakopoulos, Qing Zeng, “A three-dimensional dynamic analysis scheme for the interaction between trains and curved railway bridges”, Department of Civil and Environmental Engineering, The Hong Kong University of Science and Technology, Hong Kong, Comput. Struct., vol.149, 2015.

[19] Anil K. Chopra, “Dynamics of structures: Theory and applications to earthquake engineering”, University of California at Berkeley, 4th edition, pp. 48-50, 2012.

[20] Ehab Ellobody, “Finite element analysis and design of steel and steel – concrete composite bridges”, Department of Structural Engineering, Faculty of Engineering, Tanta University, 2nd edition.

[21] Paulius Bucinskas, Liuba Agapii, “Dynamic analysis of a bridge structure exposed to high speed railway traffic”, Aalborg University, School of Civil Engineering and Science, 2015.

[22] Jingrui Yang, Rui Duan, “Modelling and simulation of a bridge interacting with a moving vehicle system”, Department of Mechanical Engineering, Blekinge Institute of Technology, pp. 12-57, 2013.

[23] William F. Milliken, Douglas L. Milliken, "Race car vehicle dynamics", SAE International, 5th edition, 1995.

[24] Derek Seward, "Race car design", PALGRAVE, 1st edition, 2014.

[25] Mohamed Kamel Salaani, "Analytical tire forces and moments model with validated data", SAE International, SAE Technical Papers, 2007-01-0816, pp. 7-10, 2007.

[26] Edward M. Kasprzak, Kamper E. Lewis, Douglas L. Milliken, "Tire asymmetries and pressure variations in the Radt/Milliken nondimensional tire model", Society of Automotive Engineers, Inc., 2006-01-1968.

[27] John C. Dixon, "Suspension geometry and computation", 1st edition, pp. 65-97, 2009.

[28] Rouelle Claude, "OptimumG: Applied vehicle dynamics seminar", 2015.

[29] Rouelle Caude, Ariel Avi, "OptimumG: Technical papers".

[30] Massimo Guiggiani, "The science of vehicle dynamics: Handling, braking and ride of road and race cars", Springer Science+Business Media Dordrecht 2014, pp. 1-82.

[31] Reza N. Jazar, "Vehicle dynamics: Theory and applications", Springer Science+Business Media, LLC, pp. 519-973, 2008.

[32] Claudio Gomes Fernandes, Eduardo Peres, "Tire modeling for model validation", SAE Technical Papers, 2004-01-3332, 2015.

[33] Bc. Marek Urban, "Design of formula student wheel suspensions", Brno, 2020.

[34] Mike Blundell, Damian Harty, "The multibody systems approach to vehicle dynamics", Elsevier Butterworth-Heinemann, 1st edition, pp. 75-127, 2004.

[35] Altair Engineering Inc., "eBook: Learn multibody simulation with Altair MotionSolve™".

[36] Vivan Govender, David C. Barton, "Multibody system simulation and optimization of the driving dynamics of a Formula SAE Race Car", SAE International, 2009-01-0454.

[37] Altair One: Altair e – Learning, Product Documentation.

Appendix A

Yaw moment analysis and its influence on the FSAE vehicle balance

Yaw Moment is actually the resultant moment around the vertical axis that passes through the center of gravity of the car. It is the outcome of all forces acting on the contact patch when the vehicle follows a curved path. This topic is extensively described by Milliken&Milliken "Race Car Vehicle Dynamics" [23] and Optimum G [28 – 29]. Basically, the vehicle is set in a steady state situation where either the speed or the radius remains constant as the car is driven in a circular layout. The target is the generation of a diagram of yaw moment over lateral acceleration for a combination of steering wheel and body slip angles.

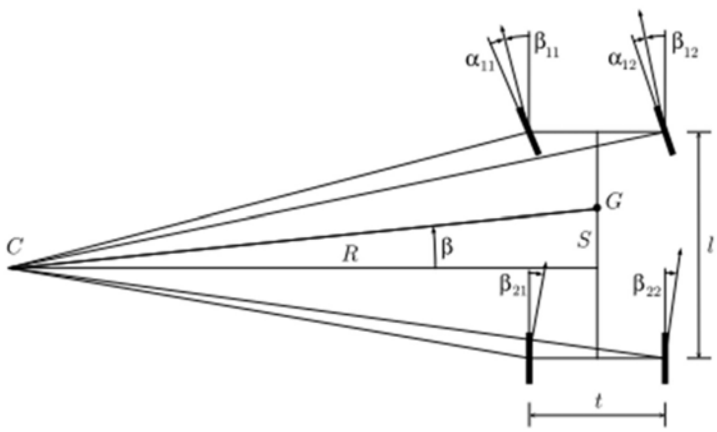

Figure A.1: Body slip and tire slip angles developed on the tires at an instant radius R

Since the initial position is for $\delta_{ij} = 0$ and $\beta = 0$, the initial normal loads (N) are calculated from static weight distribution.

$$Fz_{fl} = Fz_{fr} = \frac{m_{total} \cdot g \cdot weight\ bias_{front}}{2}$$

$$Fz_{rl} = Fz_{rr} = \frac{m_{total} \cdot g \cdot (1 - weight\ bias_{front})}{2}$$

In steady state conditions it can be assumed that the longitudinal and lateral forces as well as the self-aligning torque are functions of the following factors:

$$F_x = f(a, sr, F_z, P, ia)$$

$$F_y = f(a, sr, F_z, P, ia)$$

$$M_z = f(a, sr, F_z, P, ia)$$

where a is the slip angle, sr the slip ratio, F_z the normal load, P the tire pressure and ia the inclination angle. The Pacejka's model results to these magnitudes.

According to the documentation from these three factors that affect the yaw moment, only the lateral forces participate in a significant amount. The other two could be neglected.

The lateral force transferred in the car's CoG is the combination of four tire forces.

$$F_y = \cos(\delta) \cdot \left(Fy_{fl} + Fy_{fr}\right) + Fy_{rl} + Fy_{rr}$$

Lateral acceleration is now calculated based on the lateral force output.

$$a_y = \frac{F_y}{m_{total}}$$

The variation in lateral force causes load transfer and so the normal loads have to be recalculated.

$$Fz_{fl} = \frac{m_{total} \cdot g \cdot weight\ bias_{front}}{2} - WT_{front}$$

$$Fz_{fr} = \frac{m_{total} \cdot g \cdot weight\ bias_{front}}{2} + WT_{front}$$

$$Fz_{rl} = \frac{m_{total} \cdot g \cdot (1 - weight\ bias_{front})}{2} - WT_{rear}$$

$$Fz_{rr} = \frac{m_{total} \cdot g \cdot (1 - weight\ bias_{front})}{2} + WT_{rear}$$

Where total load transfer formulation is extensively described in section 3.5.

Note, all the above refers to a car taking a left corner.

Since the lateral acceleration results in roll angle, the inclination angles will also be different.

$$M = m_s \cdot a_y \cdot (CG_{zSM} - RC_z)$$

$$Roll\ angle = \frac{M}{K_{\Phi\ \mathrm{-Front}} + K_{\Phi\ \mathrm{-Rear}}}$$

$$ia_{fl} = Roll\ angle \cdot ia_{fl_0}$$

$$ia_{fr} = Roll\ angle \cdot ia_{fr_0}$$

$$ia_{rl} = Roll\ angle \cdot ia_{rl_0}$$

$$ia_{rr} = Roll\ angle \cdot ia_{rr_0}$$

Here inclination angles should be further adjusted due to camber variation coming from steering system.

Finally, the yaw moment is formulated combining all the above.

$$N = Yaw\ inertia \cdot Yaw\ acceleration$$

$$N = \left(F_{y_{fl}} + F_{y_{fr}}\right) \cdot \cos\delta \cdot l_f + F_{y_{fl}} \cdot \sin\delta \cdot \frac{t_f}{2} - \quad F_{y_{fr}} \cdot \sin\delta \cdot \frac{t_f}{2} - \left(F_{y_{rl}} + F_{y_{rr}}\right) \cdot \frac{t_r}{2}$$

Now, the new yaw rate for the slip angles calculation is calculated from lateral acceleration.

$$r = a_y \cdot R$$

The Yaw Moment computation is an iterative process that is terminated when the extracted yaw rate difference satisfies a given tolerance. The output of this procedure is the Yaw Moment Diagram.

Oversteering – Understeering

The yaw moment is strictly connected with the behavior of the car in a corner. Any corner could be split in five phases.

→ Entry

→ Entry - Apex

→ Apex

→ Apex - Exit

→ Exit

The way the car will turn can be described by measuring its yaw moment in each phase.

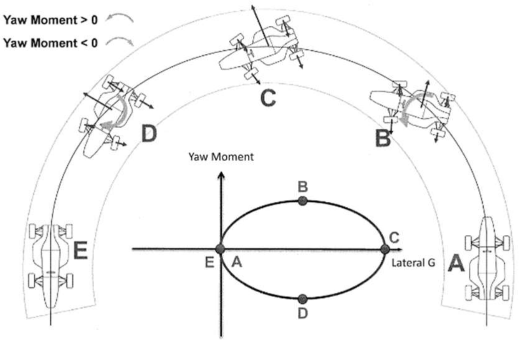

Figure A.2: Corner phases of yaw moment (Picture is taken from Optimum G seminar notes)

A: Lateral acceleration and yaw moment are zero.

A-B: Driving from A to B a positive yaw moment has to be generated to lead the car in the inner of the corner.

B: Maximum positive yaw moment is generated.

B-C: Driving from B to C the amount of yaw moment has to be reduced since it is driven towards the apex of the corner.

C: It is the corner apex, where maximum lateral acceleration is achieved. The yaw moment here should be zero for a steady state cornering.

C-D: Negative yaw moment is required to make the car exit the corner.

D: Point of the corner where the yaw moment reaches maximum negative value.

D-E: Yaw moment starts increasing until finally becomes equal to zero at corner exit.

E: Yaw moment and lateral acceleration are zero again and the car is in straight position.

The maximum lateral acceleration a car can achieve is the maximum grip it can produce at the apex.

Apex is quite an important phase, since the amount of yaw moment at this stage is not always equal to zero, as the steady state situation demands. If front tires develop greater lateral acceleration than the rear, the front of the car turns too much in the corner. An excess of yaw moment at this phase is observed and this results in an oversteering car. On the other hand, if the front tires have less grip than the rear tires, the car cannot follow the corner layout and turns widely. The front of the car tends to go outside the turn. The result is a lack of yaw moment at this phase, leading to an understeering car. The amount of yaw moment in the apex of the turn is defined as balance.

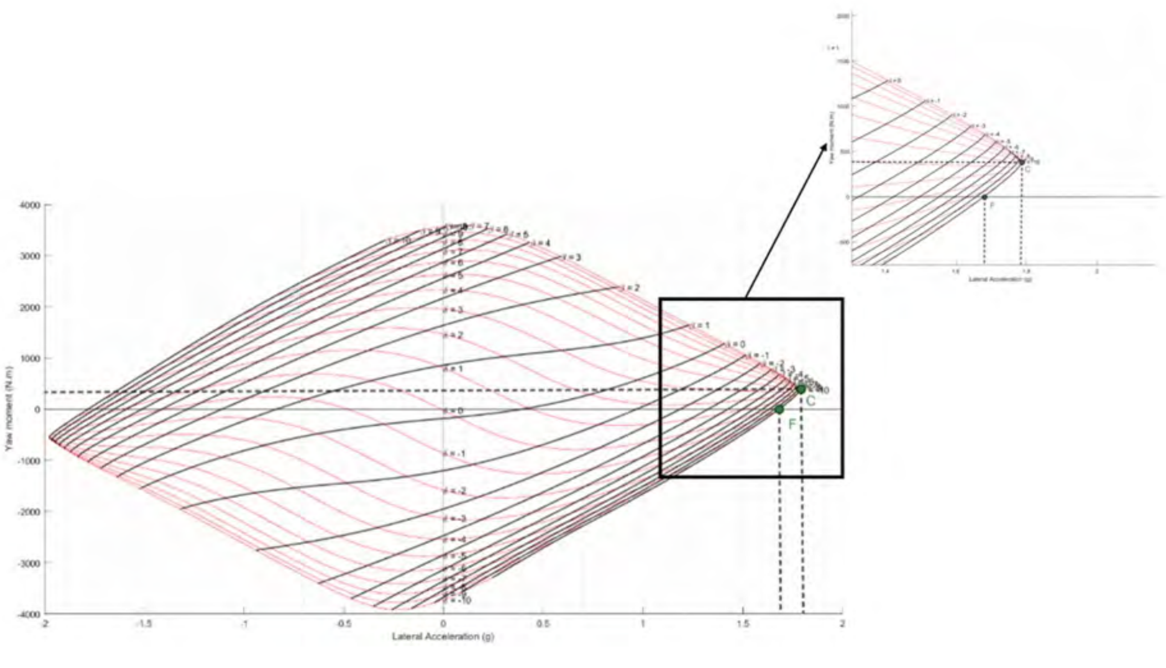

Figure A.3: Yaw moment diagram

From the diagram it is clear the maximum available grip of the car. If the maximum acceleration is reached the vehicle tends to oversteer. This corresponds at point C. However, if a neutral handling is targeted, the maximum acceleration should be as indicated from the point F.

The black curves represent the stability which is the partial derivative of yaw moment with respect to the body slip angle. The lower the magnitude, the more stable the car is.

$$Stability = \frac{\partial N}{\partial \beta} \qquad [\frac{Nm}{deg}]$$

The red lines represent the control which is the partial derivative of yaw moment with respect to the steering angle. The higher the magnitude, the more controllable the car is.

$$Control = \frac{\partial N}{\partial \delta} \qquad [\frac{Nm}{deg}]$$